DOKUZ EYLÜL UNIVERSITY

GRADUATE SCHOOL OF NATURAL AND APPLIED SCIENCES

PRODUCTION OF NICKEL OXIDE SPUTTERING TARGETS FOR HOLE TRANSPORT LAYERS IN PEROVSKITE SOLAR CELLS

by

Begüm UZUNBAYIR

January, 2021

İZMİR

PRODUCTION OF NICKEL OXIDE SPUTTERING TARGETS FOR HOLE TRANSPORT LAYERS IN PEROVSKITE SOLAR CELLS

A Thesis Submitted to the
Graduate School of Natural and Applied Sciences of Dokuz Eylül University
In Partial Fulfillment of the Requirements for the Degree of Master of Science in Metallurgical and Materials Engineering

by

Begüm UZUNBAYIR

January, 2021
İZMİR

M.Sc THESIS EXAMINATION RESULT FORM

We have read the thesis entitled "**PRODUCTION OF NICKEL OXIDE SPUTTERING TARGETS FOR HOLE TRANSPORT LAYERS IN PEROVSKITE SOLAR CELLS"** completed by **BEGÜM UZUNBAYIR** under the supervision of **ASSOC. PROF. DR. MUSTAFA EROL** and we certify that in our opinion it is fully adequate, in scope and in quality, as a thesis for the degree of Master of Science.

Assoc. Prof. Dr. Mustafa EROL

Supervisor

Assist. Prof. Dr. Serdar YILDIRIM

Jury Member

Assoc. Prof. Dr. Fethullah GÜNEŞ

Jury Member

Prof.Dr. Özgür ÖZÇELİK

Director

Graduate School of Natural and Applied Sciences

ACKNOWLEDGMENTS

In my exhausting and stressful but enjoyable journey to my Master's degree, there have been so many collaborators and encouraging people that without them it would be impossible. I would like to express my sincere thanks to all of them.

First and foremost, I would like to express my deepest appreciation to my thesis advisor Assoc. Prof. Dr. Mustafa EROL. I consider him as an exemplary mentor who motivated and taught me how to conduct research effectively by maintaining a work-life balance. Last but not least, it would be impossible to finish this research without his constructive ideas, help, constant support, guidance, and contributions.

I would also like to thank my committee members, Assist. Prof. Dr. Serdar YILDIRIM and Assoc. Prof. Dr. Fethullah GÜNEŞ for reviewing my work and offering valuable suggestions and sharing their visions about the content of my thesis.

I would like to thank Salih Alper AKALIN and Dr. Sibel OĞUZLAR, whom I had the chance to work on the project, for their guiding shares in my studies, their assistance in the analysis, and their moral support in my education process. We spent so much time doing research together and all of you have taught me, guided me, helped me, and laughed at me so much. I loved it. Also, I would like to thank Dokuz Eylül University Electronic Materials Production and Application Center and its staff for the opportunities they offered me. I also would like to thank the employees of Katip Çelebi University Central Research Laboratory for helping me with the analysis I would like to appreciate Saadet GÜLER for his encouragement, and help. I would like to thank my dear graduate friends, Uğur KARTAL, who made my working environment more active and more enjoyable during my graduate period.

I would like to express my gratitude to Dokuz Eylül University Scientific Research Projects Coordination Unit (DEU-BAP) for the support and opportunities they provided to my master's thesis, which was carried out within the scope of the project named "Production and Development of Hole Transport Materials in New Generation Perovskite Solar Cells" with the code of 2019.KB.ML T.004.

I give my thanks to The Scientific and Technological Research Council of Turkey (TUBITAK-ARDEB) for their support on a project of the Career Development Program (3501, Project Number: 118M621) called “Development of Hierarchical Graphene/α-Fe_2O_3 Nanocomposites as Glucose Biosensors”. I would also like to thank TUBITAK-BIDEB for the student scholarship support they provided within the scope of the "2210-C Domestic Postgraduate Scholarship Program for Priority Areas".

Finally and most importantly, none of this could have happened without my family. My mother Fatma UZUNBAYIR deserve very special thanks for her invaluable love, continuous support, and encouragement when I had to experience some up and downs during my study. Also, I must express thanks to my brother Berkant UZUNBAYIR for providing me with his unfailing support, encouragement, and sense of humor. And my dad, Adem UZUNBAYIR, you are always in my heart with deep love and I will always try to be a human you will be proud of.

Begüm UZUNBAYIR

PRODUCTION OF NICKEL OXIDE SPUTTERING TARGETS FOR HOLE TRANSPORT LAYERS IN PEROVSKITE SOLAR CELLS

ABSTRACT

Perovskite solar cells have been an interesting subject of research in recent years due to their low production cost, their ability to allow a wide variety of design changes, and the high efficiency they reach in a short time. Inorganic p-type semiconductors used as hole transport material, a crucial layer in perovskite solar cells, have high transparency, structural stability, and adjustable band gaps. Nickel oxide (NiO_x) stands out compared to other inorganic hole transport material with its high thermal and chemical stability, optical transparency, wide bandgap (3.6 - 4.0 eV), low material cost.

In the thesis, the target materials obtained for deposition of NiO_x thin films that are desired to be used as hole transport material, consist of powders produced by sol-gel method. The pristine and lithium-doped NiO_x powders were successfully produced by the sol-gel method. The NiO_x based powders were preformed into NiO_x target materials with a bulk density of 95 percent and above, using an isostatic press. Then the obtained target materials were used in the RF magnetron sputtering system to produce NiO_x thin films. The thicknesses of films, which were successfully deposited on the glass/ ITO substrate, were measured between 110- 230 nm. Consequently, the obtained target materials exhibited promising for the production of thin films that can be used in perovskite solar cells. At the end of each production step, the materials were structurally and morphologically characterized by relevant characterizations such as X-ray diffraction, X-ray photoelectron spectroscopy, scanning electron microscopy, particle size distribution, and density measurement.

Keywords: Perovskite solar cells, hole transport material, nickel oxide, target materials

PEROVSKİT GÜNEŞ PİLLERİNDE BOŞLUK TAŞIMA KATMANLARI İÇİN NİKEL OKSİT SAÇTIRMA HEDEF MALZEMELERİNİN ÜRETİLMESİ

ÖZ

Perovskite güneş pilleri, düşük üretim maliyetleri, çok çeşitli tasarım değişikliklerine izin verme kabiliyetleri ve kısa sürede ulaştıkları yüksek verimlilik nedeniyle son yıllarda ilginç bir araştırma konusu olmuştur. Perovskit güneş pillerinde önemli bir katman olan boşluk taşıyıcı malzemesi olarak kullanılan inorganik p-tipi yarı iletkenler, yüksek şeffaflığa, yapısal kararlılığa ve ayarlanabilir bant boşluklarına sahiptir. Nikel oksit (NiO_x), yüksek termal ve kimyasal kararlılığı, optik şeffaflığı, geniş bant aralığı (3,6 – 4,0 eV), düşük malzeme maliyeti ile diğer inorganik boşluk taşıyıcı malzemelere göre öne çıkmaktadır.

Tezde boşluk iletim malzemesi olarak kullanılması istenen NiO_x ince filmlerin biriktirilmesi için elde edilen hedef malzemeler, sol-jel yöntemi ile üretilen tozlardan oluşmaktadır. Saf ve lityum katkılı NiO_x tozları, sol-jel yöntemi ile başarıyla üretildi. NiO_x esaslı tozlar, izostatik bir pres kullanılarak yüzde 95 ve üzeri yığın yoğunluğuna sahip NiO_x hedef materyalleri haline getirildi. Daha sonra elde edilen hedef malzemeler, NiO_x ince filmler üretmek için RF magnetron püskürtme sisteminde kullanıldı. Cam / ITO substratı üzerine başarıyla yerleştirilen film kalınlıkları 110- 230 nm arasında ölçüldü. Sonuç olarak, elde edilen hedef malzemeler, perovskite güneş pillerinde kullanılabilecek ince filmlerin üretimi için umut vaat etmektedir. Her üretim aşamasının sonunda, malzemeler yapısal ve morfolojik olarak X-ışını kırınımı, X-ışını fotoelektron spektroskopisi, taramalı elektron mikroskobu, parçacık boyutu belirleme ve yoğunluk ölçümü gibi ilgili karakterizasyonlarla karakterize edildi.

Anahtar Kelimeler: Perovskit güneş hücreleri, boşluk taşıyıcı malzeme, nikel oksit, hedef malzemeleri

CONTENTS

Page

LIST OF FIGURES

Page

LIST OF TABLES

Page

CHAPTER ONE
INTRODUCTION

The energy need of humans is increasing day by day due to the increasing population, developing technology, and the relative increase of the living standards. In addition, the limited amount of fossil fuels and their damage to the environment such as global warming of CO_2 emissions is pushing the world towards developing and using renewable energy sources. Nowadays, renewable energy sources (solar, wind, hydroelectric, geothermal, etc.) have been helping to overcome these problems. In this context, solar energy has become one of the rapidly developing sources of renewable energies in the world due to its inexhaustible and easily accessible properties both on earth and in space. The solar cells generally convert sunlight, falling on their surfaces, into electrical energy depending on their functional layers and their structural, electronic, and optical properties. Simply summarized, solar cells are devices that convert solar energy into electrical energy. When the development of solar cells from the past to the present is examined, in cell selection; the structure, cost, stability, and efficiency of the cell come to the fore. As a result of this development, solar cells are defined as 3 different generations depending on the material type, production method, cost, and design.

1st generation solar cells are silicon and germanium based and they are inelastic (rigid) structures. The efficiency of 1st generation solar cells, which is the most used type commercially, is high. 2nd generation solar cells, also known as thin-film solar cells, are structures using amorphous silicon (a-Si), copper indium gallium selenide (CIGS), or cadmium telluride (CdTe) materials. Considering the demanding production conditions of 1st generation cells, thin-film solar cells can be produced in large sizes on economical substrates made of glass, polymer or metal derivatives. Thus, cells can be developed at a low cost, suitable for mass production, and flexible when required. On the other hand, the low reserves of the starting materials needed in production and their toxic effects limit their use (Ranabhat et al., 2016). 3rd generation solar cells are generally in the form of multi-layer thin film structures (DSSC - dye sensitive solar cells, PSC - perovskite solar cells) consisting of different material types using small molecules and/or polymers. When the process efficiency improvement of

these cells was evaluated compared to the 1st and 2nd generation cells, they reached their present location in a very short time since their first development. PSCs, which have attracted the attention of researchers for the past decades, have reached a theoretical efficiency of 22.7 ± 0.8% today (Zheng et al., 2018). These cells, which have the potential to increase efficiency with various changes to be applied in the multilayer structure, are still in the laboratory stage today due to their stability problems. For this reason, it lagged behind the 1st and 2nd generation cells in terms of mass production and commercialization.

PSCs in which organo-metal halide perovskites are used are basically composed of three main layers: hole transport material (HTM), absorber material (Psk), and electron transport material (ETM). Among these layers, ETM and HTM, which show n-type and p-type semiconductor properties, provide the movement of electron and hole pairs formed by photons falling on the absorbing Psk layer. Apart from these main layers, the cell contains a transparent conductive oxide (TCO) layer and a metallic layer (ME) in a transparent conductive structure that allows light penetration to connect with the external circuit. HTMs are semiconductor materials showing the p-type character that enable hole movement in solar cells. In order for these semiconductor materials to be used as HTM, band gap values, optical properties, charge-carrying, and electron blocking properties are important. Also, in order for the cell to work, the transmission band energy value of HTMs must be compatible with the value of the Psk layer. Both organic (spiro-MeOTAD, PEDOT: PSS, PTAA, PCBM, etc.) and inorganic (NiOx, CuSCN, CuI, etc.) materials are used as HTM in perovskite solar cells. Due to the properties of organic HTMs such as high acidity, water absorption tendency (hygroscopicity), an inadequate electron blocking feature, high cost, and complex synthesis steps, it prevents the commercialization of PSCs (Fu et al., 2018). Organic HTM's; Exposure to environmental conditions, humidity, and UV-visible light during operation disrupt the structure and stability of these materials. Therefore, inorganic HTMs, which are more suitable for working conditions and open to development, are preferred in recent years. Among them, nickel oxide (NiO_x) stands out thanks to its properties such as high thermal and chemical stability, optical transparency, wide bandgap (3.6 - 4.0 eV), and low material cost (Chen & Park, 2018).

In this study; It was produced as pristine and Li-doped NiO_x powder by sol-gel method and then these powders were transformed into target materials to be used in the magnetron sputtering method with the help of the cold isostatic press. These target materials were used during the deposition of the HTM layer on glass / ITO with the magnetron sputtering method. After the productions have been carried out, relevant analyzes are made and the materials are characterized.

As a general introduction in Chapter 2, photovoltaic cells, their classification, layers of perovskite solar cells and their properties, the working principle of solar cells, thin-film production methods, and powder metallurgy are explained. Chapter 3 summarizes the studies on NiO_x, an inorganic HTM in the literature. In addition, general information about NiO_x and its additive element lithium has been given. Chapter 4 contains details of the experiment. All characterization techniques and applications are briefly explained. In Chapter 5, the general results of characterization and application studies are given and interpreted. The results obtained were discussed with similar studies reported. Finally, the overall results of this study and the future plans for the study are presented in Chapter 6.

CHAPTER TWO
THEORITICAL BACKGROUND

2.1 A Brief Introduction to Solar Cells

The solar cells generally convert sunlight, falling on their surfaces, into electrical energy depending on their functional layers and their structural, electronic, and optical properties. When the development of solar cells from the past to the present is examined, cell structure, cost, stability, and efficiency come to the fore in cell selection. As a result of this development, solar cells are divided into three categories called generation depending on the material type, production method, cost, and design.

The 1st generation solar cells are silicon and germanium based and they are inelastic (rigid) structures. Silicon is currently the most widely used material in semiconductor technology, and the cells produced with this material still dominate 95% of the photovoltaic energy market worldwide (Woodhouse et al.,2017). The production of Si-based materials is commonly achieved using the Czochralski method. In this method, cylindrical ingots are produced by melting silicon pieces (> 99.999% purity) at high temperatures in a quartz crucible and solidifying directly from the liquid with controlled drawing and rotation speeds in the magnetic field. After various slicing and surface treatments, the obtained ingots are transformed into the final product with a wafer whose crystal orientation can be controlled, and then by coating and lithography operations (Anttila, 2015). Silicon used in photovoltaic cells can be preferred in single-crystalline and polycrystalline forms. While the highest reported efficiency of polycrystalline solar cells from 1st generation photovoltaic cells is 22.3%, the highest reported efficiency of single crystal solar cells is 26.7%. In general, single crystal-based cells turn into solar cells as a result of processes such as forming p-n joints on wafers by diffusion, deposition of anti-reflective layers, forming metallic junction points but these processes are time-consuming and expensive (Philipps et al., 2018).

The 2nd generation photovoltaic cells, also known as thin-film photovoltaic cells, are structures using amorphous silicon (a-Si), copper indium gallium selenide (CIGS), or cadmium telluride (CdTe) materials. Considering the demanding production conditions of the 1st generation cells, thin-film solar cells can be deposited on

economical substrates from glass, polymer, or metal derivatives in large size. Thus, these cells; have low production costs, are suitable for mass production, and can be produced in flexible forms when required. On the other hand, the low reserves and toxicity of the starting materials such as Cd, Te, Se, etc. limit their application. (Ranabhat et al., 2016). In thin-film solar cells, the semiconductor material has a direct bandgap in opposite to the indirect bandgap of crystalline silicon, but still, these devices rely on a p-n junction structure. A top layer named the window layer consisting of a large bandgap material absorbs the high energy photons, while a bottom layer named the absorber layer consisting of a small bandgap material absorbs the low energy photons. This structure allows for intrinsically better efficiency (Oflaz, 2019).

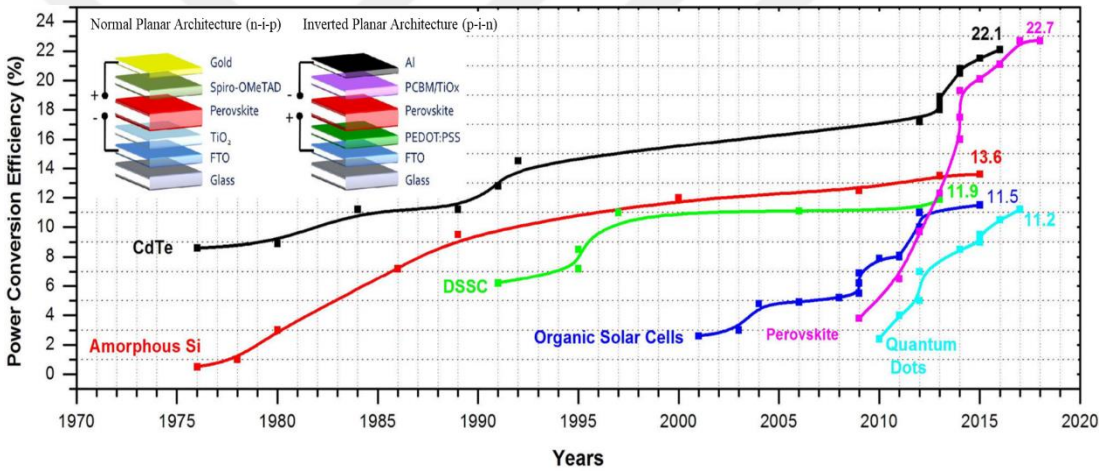

Figure 2.1 The progress of power conversion efficiency of perovskite-based solar cells compared with other types of solar cell technologies. The n-i-p and p-i-n structure is demonstrated in the subset figure (Hamed & Mola, 2020)

The 3rd generation photovoltaic cells such as dye-sensitized solar cells (DSSCs), organic quantum dot solar cells, perovskite solar cells (PSCs) are younger members of the solar cell family. These devices are constituted from small molecules and/or polymers which are used generally as a thin film form. When the process efficiency improvement of these cells was evaluated compared to the 1st, 2nd, and 3rd generation cells, PSCs reached their present location in a very short time since their first development, as can be seen in Figure 2.1. Various studies are carried out on the

development of high-efficiency perovskite fabrication and optimization of the production process of PSCs. As a result of these studies, PSCs showed a rapid rise with a record efficiency reaching up to 22.7 % as a result of benign properties of the material such as strong optical absorption, long diffusion lengths, and solution processability (Zheng et al., 2018).

2.2 Functional Materials of Perovskite Solar Cells

The development of new materials for use in cells and a more in-depth understanding of the working principles of perovskite structures have led the development of perovskite solar cells. Along with these, both the architecture of the general perovskite solar cell and the selection of the materials have a considerable influence on the development of electronic and optical properties of the device. The materials namely layers in perovskite solar cells can be categorized into five groups: the transparent conductive oxide (TCO) layer, the electron transport material (ETM), the photoactive perovskite material (Psk), the hole-transport material (HTM), and the metal contact material. For solar cell development, suitable HTMs and ETMs must have well-matched valance band (VB) and conduction band (CB) energy levels with perovskite. In Figure 2.2, the energy level graph for various functional layers (ETMs, Psks, HTMs, anode, cathode) is given.

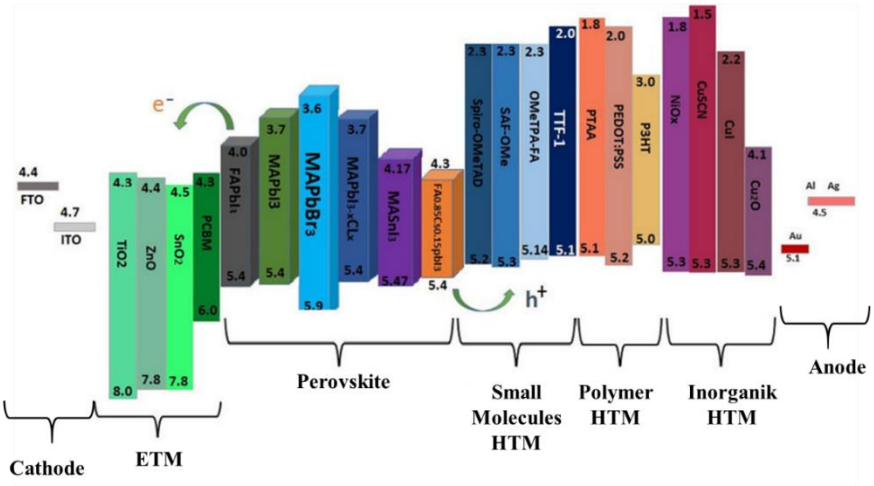

Figure 2.2 Representation of the energy levels, for cathode materials, n-type ETMs, perovskites, p-type HTMs, and anode materials from left to right (Hamed & Mola, 2020)

2.2.1 Transparent Conductive Oxides

Due to their conductivity and optical transparency, transparent conductive oxides are used as electrodes in PSCs so as to provide electrical connection and light penetration. Besides, they can be deposited as thin films on different surfaces such as glass, polyethylene terephthalate (PET). Flexible substrate applications as PET are suitable for PSCs because it allows the device to be more lightweight and bendable compared to glass or other rigid substrates. Optical transparency, smooth running functionality, and low layer resistance are shown as important properties for TCOs. For solar cell application, TCOs should have a bandgap of 3.1 eV or higher to transmit 80 % of the visible light (Sarialtin et al., 2020).

The most common types of TCO films are fluorine-doped tin oxide (FTO) and indium tin oxide (ITO). Although TCOs are used for the same properties in applications, their properties such as surface roughness and surface wettability differ from each other. It has been reported that due to the low coverage of the films made on ITO, ITO-based solar cells exhibit lower performance compared to FTO-based devices (Oflaz, 2019). Studies have shown that ITO has many advantages in terms of ohmic behavior and conductivity. FTO is generally used in thin-film solar cell applications due to its crystallinity and electrical conductivity performances and cost advantage (Sarialtin et al., 2020).

2.2.2 Electron Transport Materials

The main function of the electron transport layer is to create an electron-selective contact with the perovskite light-absorbing layer to improve the efficiency of the electron-gap charge separation generated by light and reduce recombination, effectively preventing the hole from passing to the opposite electrode. Metal oxide n-type semiconductors such as ZnO, SnO_2, and TiO_2 are generally used as the electron transport layer. In particular, TiO_2, with its wide bandgap, is the most widely used and studied electron transport material. Many studies have focussed on the effects of different n-type semiconductor materials and structures on power conversion

efficiency (Shi & Jayatissa, 2018). Besides inorganic ETMs, PCBM (one of the fullerene derivatives, [6,6] -phenyl-C61-butyric acid methyl ester) and PFN (poly [9,9-dioctylfluorene-9,9-bis (N Organic ETMs such as, N-dimethylpropyl) fluorene]) are also used. The organic alternatives are flexible and solution processible but not cost-effective if compared. The general properties of electron transport materials to be selected should be as follows.

- It is recommended to use n-type semiconductors with high carrier mobility.
- ETM must be both wide-range bandgap and transparent to visible light.
- Mild preparation conditions should be chosen so that the material can be obtained at low temperatures.
- The band energy level of the perovskite material and the band energy level of the material used for ETM must be in harmony.

2.2.3 Perovskite Absorber Materials

Among all functional layers of perovskite solar cells, perovskite materials play an important role in light absorption and photoelectric conversion. ABX_3 perovskite compounds, which form the basis of PSCs, were discovered by the Russian mineralogist Perovski in 1839 (Etgar, 2016a). The perovskites were used as an absorbent layer in PSCs consist of organic and inorganic structures. In ABX_3 structures is shown Figure 2.3, A is referred to as a monovalent organic/ inorganic cation is usually methyl ammonium ($CH_3NH_3^+$) or formamidinium (NH_2-CH_2=NH_2^+); B is usually a divalent inorganic (metal) cation (Pb^{2+} or Sn^{2+}), and the X portion is the I^-, Cl^-, or Br^- anions.

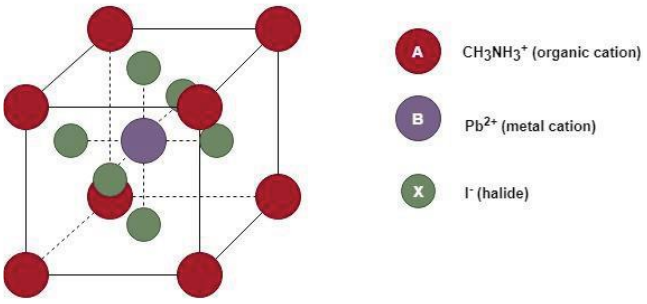

Figure 2.3 The unit cell demonstration of a perovskite crystal structure; ABX_3

Interest in halide perovskites increased when Mitzi et al. discovered that layered organo-metal halide perovskites exhibit semiconductor-metal transition with increased dimensionality (transition from two-dimensional state to three-dimensional structure). Thus, it has been found that the bandgap energy decreasing with increasing dimensionality is suitable for photovoltaic applications (Mitzi et al., 1994). However, other perovskite materials such as mixed cation, mixed halide, and mixed halide–mixed cation perovskites are attracting increasing attention since they have some advantages over the traditional $MAPbI_3$ perovskite. The adjustment combinations of anions and cations cause changes in perovskite crystal size, band gap energy level, stability, and device performance. The unique structure of perovskite; low exciton binding energy, high absorption coefficient, adjustable band gaps, high charge-carrier mobility, and long hole and electron diffusion lengths (Etgar, 2016).

2.2.4 Hole Transport Materials

The main role of p-type HTMs is to collect and transport holes from the electron-hole pair formed in the perovskite absorber layer and to promote electron-hole separation by working in collaboration with n-type ETMs. The HTMs to be selected in the PSC application must have some suitable characteristics to work properly;

- It should provide hole conduction from the electron-hole pair formed in the perovskite layer, and prevent electron conduction by acting as a barrier between the anode and the perovskite layer. That is, the lowest empty molecular orbital energy level for organics, and the valence band energy for inorganics should be significantly lower than that perovskite material.
- HTMs should have high hole transfer efficiency both to facilitate hole transmission and to prevent recombination of separated electron-hole charges.
- There should be no diffusion between the HTM layer between the perovskite material and the electrode metal.
- For long-term performance, it should not be affected by humidity and oxygen in the environment and should have high thermal stability. It should also be environmentally friendly and cost-effective (Pitchaiya et al., 2020).

HTMs are classified into two types based on the chemical compositions as organic and inorganic HTMs. The most commonly preferred organic HTM is Spiro-OMeTAD due to its good match with perovskite energy levels and higher cell performances around >20% PCE (X. Li et al., 2016). In the class of organic HTMs, some polymer semiconductors with hole-selective properties have been cost-effective alternatives to spiro-OMeTAD, such as poly-triarylamine (PTAA), poly(3,4-ethylene dioxythiophene) polystyrene sulfonate (PEDOT: PSS), poly(3- hexylthiophene-2,5-ditl) (P3HT), and polyaniline (PANI) (Heo et al., 2013; Najafi et al., 2018). These organic HTMs have some disadvantages such as low mobility, high cost, complex synthesis steps, and degradation under moisture and weather conditions (Chen & Park, 2018). This problem has been tried to be solved by using highly stable and low-cost inorganic HTMs such as CuI, CuS, Cu_2ZnSnS_4, Cu_2O, CuO, $CuAlO_2$, $CuCrO_2$, $CuGaO_2$, CuSCN, NiO_x, Co_3O_4, C and its derivatives, VO_x, WO_3, MoO_x. Even among them, NiO_x-based devices showed 20% PCE, a promising solution for PSCs in commercial manufacturing and utilization at harsh conditions (Liu et al., 2018).

NiO_x based HTMs can be produced generally with two different approaches like solution-based and vapor-based. When the related studies are examined, it is seen that although solution-based structures provide good stoichiometry control, their surface roughness, mechanical properties, and homogeneity are of lower quality than vapor-based production methods (Ozkan et al., 2008). This situation decreases the electrical properties of HTM and therefore the long-term stability and efficiency of PSC. Vapor-based methods such as sputtering and evaporation whose film qualities are known to be more successful than solution-based methods generally require a target material for HTM production of PSCs (Wang et al., 2014).

2.3 Working Principles of Perovskite Solar Cells

The working principles of PSCs consist of light absorption, charge separation, charge transport, and charge collection. A schematic representation of this principle of PSCs is shown in Figure 2.4. When the photons fall on an absorber layer, it is excited by photons, which have more energy than its bandgap, forms an exciton namely an electron-hole pair. Then, generated free electron-hole pairs are collected by an ETM

and HTM. Depending on the device architecture, electrons are transferred from the Psk absorber materials to the metal electrode either they are in the p-i-n structure, or the n-i-p structure, then they are transferred to TCO. Finally, the TCOs and metal electrodes are connected and the photocurrent is generated in the outer circuit.

In this process (Figure 2.4), some unwanted process may obtain, including the recombination of the generated electron-hole pairs (4), back electron and hole charge transfer at the interfaces of the ETM and HTM with absorber materials (5, 6), and the recombination caused by the direct contact between ETM and HTM (7). As a result, other generated charges can be transferred from the selective functional materials to the electrodes, and finally, the photocurrent is obtained.

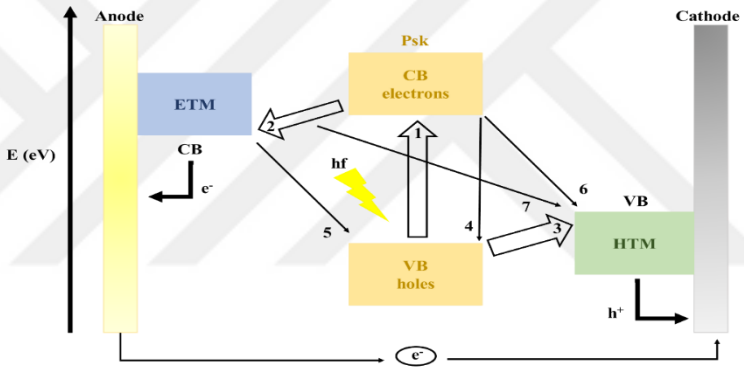

Figure 2.4 Schematic representation recombination and charge extraction events occurring in perovskite solar cell

2.4 Thin Film Deposition

Thin film technology; can be defined as the process of coating and/or depositing materials on certain substrates for different purposes using various techniques, mostly at nano levels (1-100 nm). This technology has many advantages as listed below.

- Minimizing the size of manufactured devices and equipment,
- Increasing the performance of these devices and equipment and
- Less raw material consumption
- Protection of scarce materials (Sönmezoğlu et al., 2012).

There are many thin film deposition techniques such as sol-gel hydrothermal synthesis, electrochemical, physical vapor deposition (PVD), and chemical vapor deposition (CVD). These techniques can be divided into three groups as given in Figure 2.5 as film growth in vapor, liquid, and solid states. Among these groups, vapor state film growth methods offer superiority over the other two groups because they provide controllable morphology, composition, thickness, and surface properties. The distinction between PVD and CVD, the vapor deposition methods, is in the way of vapor deposition. In PVD, steam consists of atoms and molecules that simply condense on the substrate, and in CVD, the steam goes into a chemical reaction resulting in a thin film on the substrate.

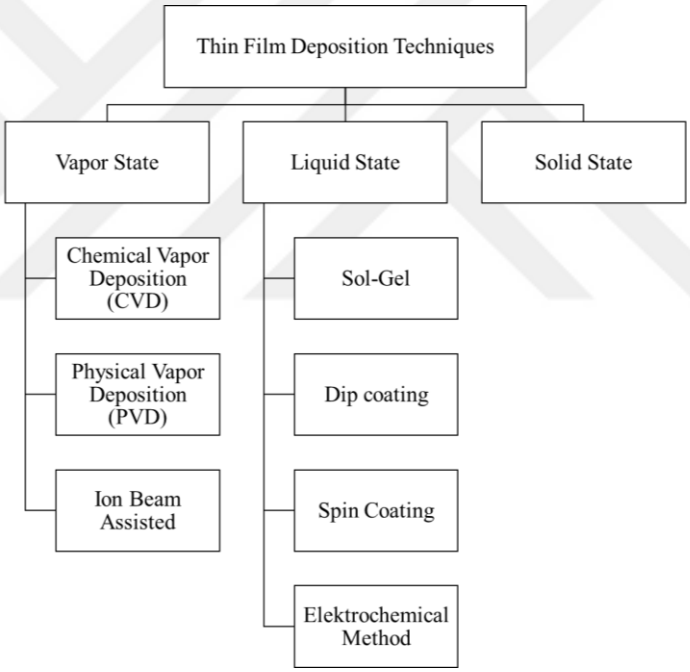

Figure 2.5 Thin-film production methods

The PVD technique, which is the vapor-phase deposition method, is one of the vapor-phase film deposition techniques based on the removal of atoms from the target material surface by evaporating or scattering materials under vacuum, and depositing them atomically or ionically on the surface of the material used as a base. Physical vapor deposition processes are basically divided into two groups as evaporation and sputtering as shown in Figure 2.6. In general, in both methods, the process takes place

by applying a negative potential (Bias) to the mass and ionizing the atoms (Jameel, 2015).

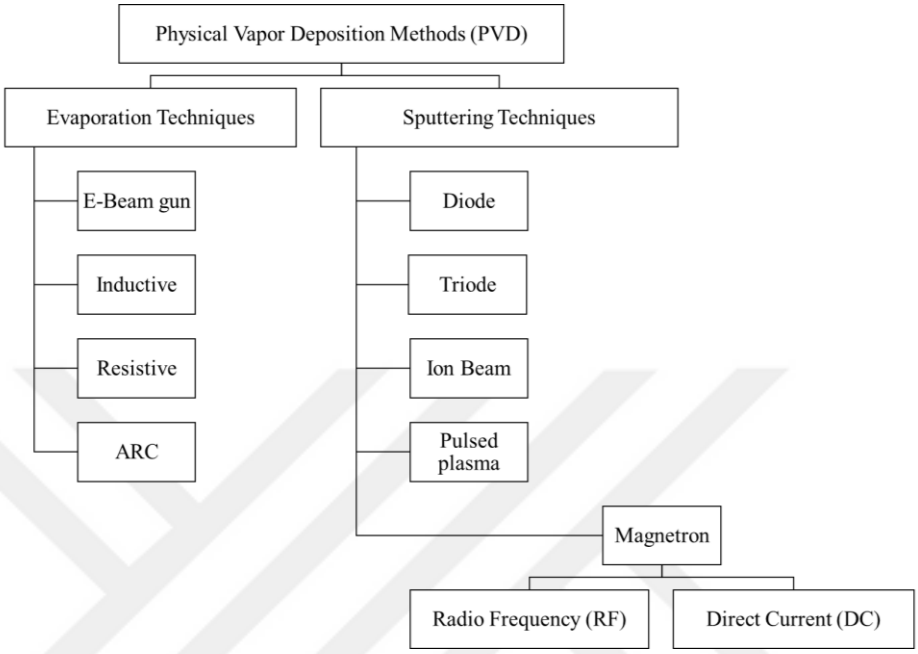

Figure 2.6 The physical vapor deposition methods with evaporation and sputtering subgroups

2.4.1 Radio Frequency (RF) Magnetron Sputtering Methods

Sputtering, one of the physical vapor deposition methods, is in principle the process of removing the atoms from the surface of a target material by ionized and accelerated gas atoms by applying voltage and throwing them onto a substrate surface. Unlike evaporation, the source is not thermally based but created by the ion effect on the target. Also, the distance between the target material and the substrate was shorter and in many cases outperformed other PVD processes are with greater functionality and performance such as improved adhesion and thicker film. The sputtering process is mainly carried out at low pressures (vacuum) and in an inert gas atmosphere. In the system, argon (Ar) is generally used as an inert gas, since it is heavier than other noble gases and is easily ionized. The percentage of reactive gas added to the chamber can be controlled to produce a specific stoichiometric ratio of a compound. Reactive sputtering is used whereby the deposited film is formed by a chemical reaction

between the target material and the gas introduced into the vacuum chamber. Oxides and nitrides are examples of thin films developed through reactive sputtering, where the compositions of these films can be controlled by adjusting the relative pressures of the inert and reactive gases. Argon is the main gas in most cases and the amount of reactive gas introduced into a process chamber is controlled either to obtain a certain amount of doping or to produce a fully reacted compound. The resulting accumulated thin film is different from the target. With the argon gas given to the system, electron discharge is created, and the argon in the environment is ionized and a plasma is formed. The negative voltage applied to the cathode causes argon ions to hit the target rapidly. As a result of this bombardment, the ions detached from the target material by the change of momentum are directed to the surface of the substrate (Figure 2.7). The sputtering method is also used as an abrasive for pattern identification and cleaning the surface of solid materials due to its potential to eject atoms from an electrode surface (Başalan, 2017; Ishihara, Li, Yumoto, & Akashi, 1998; Patent No. 7,575,661, 2009).

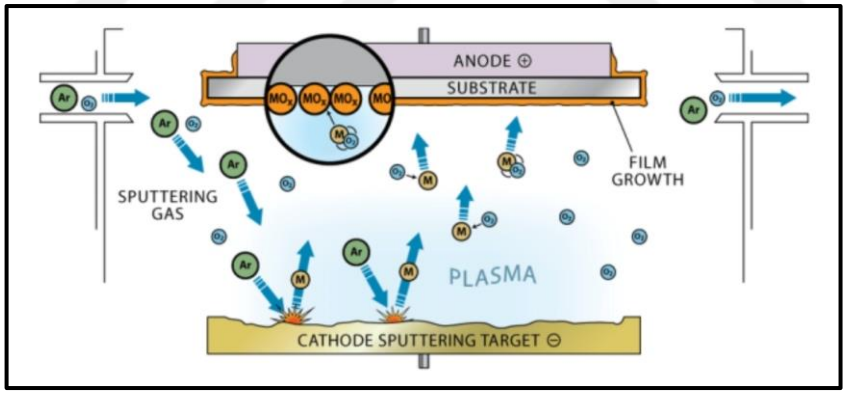

Figure 2.7 A schematic demonstration of magnetron sputter system

The most commonly used method in sputtering processes is direct current (DC) sputtering. However, in the DC sputtering process, when an insulator is used as a target material instead of a metal source, there is a problem in creating sputter discharge. For this reason, radio frequency (RF) voltage is used for deposition with insulating targets, namely insulator target materials (Gómez, Galeano, & Saldarriaga, 2015). With RF method, Si, Ti, Ge, GaAs, GaSb, GaN, AlN, CdSe, PbTe, SiC, metal oxides such as

$Bi_4Ti_3O_{12}$, In_2O_3, SiO_2, Al_2O_3, Ta_2O_5, Y_2O_3, TiO_2, ZrO_2, PtO, Bi_2O_3, ZnO, CdO, NiO, glass, and polymers can be deposited on the substrate surface (Jameel, 2015).

The sputtering system has many advantages compared to other traditional evaporation techniques. RF magnetron sputtering offers additional advantages, including the use of non-conductive targets, charge-up effects, and reduced arching due to the use of the alternating electric field. The deposition of thin films using non-conductive target materials is the most important advantage of the RF magnetron sputter system. Additionally, it does not require melting and evaporation of the source material. The high deposition rate, reduction of base material electron bombardment, the wide process vacuum range, and due to its ability to work at low pressures, it is widely available in the industry are also its other significant advantages (Maurya et al., 2014).

2.5 Target Production

2.5.1 Powder Metallurgy

Powder metallurgy (PM); is a production method that transforms metal, ceramic, and alloy powders obtained by mechanical and chemical methods into engineering parts with the help of temperature and pressure. The phase of creating a product of the PM method consists of four main steps. These are *(i) obtaining of powder, (ii) compacting the powders into preforms, (iii) sintering for providing properties,* and *(iv) post-sintering processes to final products*. In this method, firstly, metal, ceramic, and alloy powders are obtained with different production methods. The powders obtained are mixed with appropriate binding materials and pressed under pressure. Then, sintering is applied to the pressed part to provide the desired properties. As a result, production is complete (Erdoğan, 2011; Upadhyaya, 1997). The stages applied in PM production are shown in Figure 2.8.

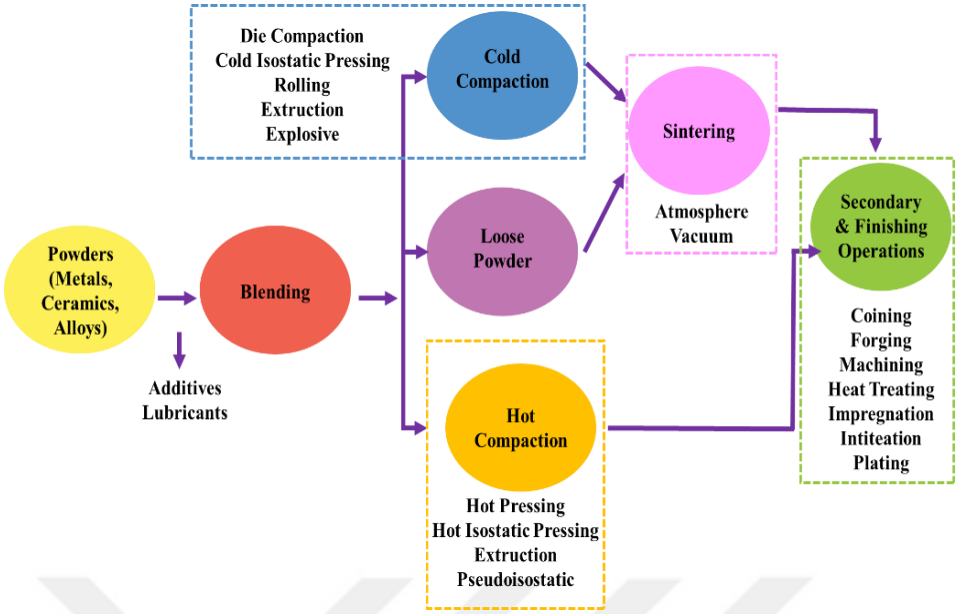

Figure 2.8 The basic steps of the powder metallurgy process

Production with PM has become a production method that is rapidly becoming widespread in developing countries due to its low cost. The significant reason for choosing the method is the economical benefit of low energy use. Powder metallurgy is highly preferred as it has advantages that are gathered under three main headings: process, metallurgical, and commercial, as well as economic benefits. (Angelo & Subramanıan, 2008).

2.5.2 Powder Production

Metal, ceramic (metal oxide), and alloy powders are the main component of PM. The powder characteristics such as size, shape, and chemical composition greatly affect both, the selection of sintering parameters and the finished PM part properties. So, a single powder production method cannot be suitable for all the applications. Therefore, many production methods to produce powders are available. These methods are divided into three main groups as mechanical, chemical, and physical methods (Figure 2.9) (Klar, 1983).

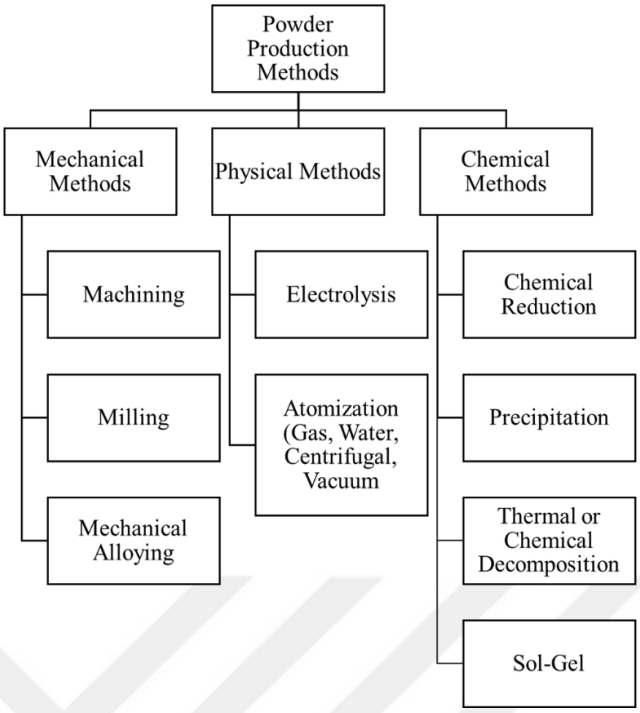

Figure 2.9 Three main groups and subgroups of powder production methods

2.5.2.1 Sol-Gel Process

The sol-gel method, which is a chemical production method, is the most preferred one in the production of PM metal oxide powders. The main advantage of this technique is that the whole process is carried out under very mild conditions (Angelo & Subramanian, 2008; Toygun et al., 2013). Thanks to this process, homogeneous inorganic oxide materials with desired properties (hardness, optical transparency, chemical resistance, porosity, and chemical resistance, etc.) can be obtained at room temperature without the need for the high melting temperature required for conversion to inorganic glasses. Besides, the ability of the sol-gel process to take place in extremely mild conditions (often at room temperature) and the ability to obtain products in various shapes, sizes, and formats have enabled this technology to take place in increasing number of applications in various scientific and engineering fields (Figure 2.10) (Toygun et al., 2013).

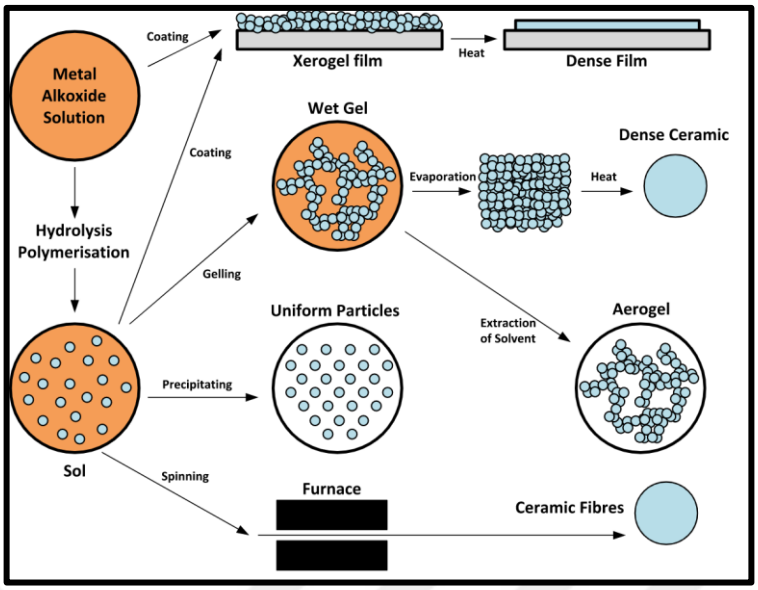

Figure 2.10 Schematic representation of the different stages and routes of the sol-gel technology (Brinker & Scherer, 2013)

The description of a sol is a stable suspension of colloidal particles inside a liquid or a solution of polymer molecules (Rahaman, 2017) For the existence of a sol, the solid particles should be denser than the liquid. Colloids are made from these solid particles, and these colloids range from 1-1000 nm (Ün, 2008). The gel is a porous and 3-dimensional state with a high-density liquid and solid dispersion, containing liquid components. The important criterion for gel formation is the bonding between the smallest solvent particles and dissolved particles.

The sol-gel process includes such main steps including hydrolysis, condensation, gelation, aging, drying, and sintering. The first step in the sol-gel process is the formation of the sol. Sol is a colloidal suspension of liquid-solid particles. Metal alkoxides ($M(OR)_x$) and inorganic salt are used as precursors in sol-gel. In the hydrolysis step, the precursors are hydrolyzed in water or, depending on the type of precursors, in the appropriate alcohol. The hydrolysis step is followed by condensation forming structures in different forms like powders, finers, thin films, amorph bulk, and monolithic solid. These forms are heat treated to get the final ceramic by removing the organic groups from the structure. The performance characteristics of the sol-gel process can be affected by many conditions. These are:

- Nature and concentration of precursors
- Type of solvent and acidity of the medium
- The concentration of each type of insolvent
- Type and concentration of additives
- The aging time of gel
- Temperature
- Heat treatments applied (Toygun et al., 2013)

Hydrolysis occurs without the addition of a catalyst. However, when the catalyst is used, the reaction can be completed much faster and more accurately. Therefore, hydrolysis and condensation processes are significantly affected by the pH of the solutions and the structure and concentration of the catalyst used. During hydrolysis, the formation of the sol structure takes place as a result of peptization. The type of acid used also affects peptization. Generally, non-complex or weak acids are effective in sol formation (Brinker & Scherer, 2013). Mineral acids (HCl) and ammonia (NH_3) are generally used catalysts. Also, acetic acid (CH_3COOH), potassium hydroxide (KOH), amines, potassium fluoride (KF), and hydrofluoric acid (HF) are used. It is known that the most important factor affecting the rate of hydrolysis reaction is the use of acid or basic catalyst. In addition, it is mentioned in the literature that the low pH of the sol increases the gelation time. It is generally accepted that the base-catalyzed sol-gel process produces a high density (strongly bonded) particle structure, while the acid catalyst produces a linearly branched polymer (bonded with light bonds) (Li et al.,2004; Toygun et al., 2013). Linear or randomly branched polymer structures are formed in the acid-catalyzed mechanism. At equal catalyst concentration, base-catalyzed reactions are slower than acid-catalyzed reactions, and grouped products are formed (Kloskowski et al., 2010). This is because the condensation reaction is faster when using the basic catalyst and the speed of the entire sol-gel process is determined by the relatively slow hydrolysis step. On the other hand, under acidic conditions, hydrolysis of the alkoxide precursor occurs faster than the condensation process. All these features make it easier for the researchers to control the research parameters to reach the configuration of the final product with the desired qualities (Ün, 2008)

Gelation can simply be explained as an agglomeration of particles or condensation of polymers until the clumps collide, growth of clusters followed by the formation of bonds between clusters to form a single large cluster. The structure formed as a result of these events is called "gel". Depending on the speed and shape of the gelation reactions, the microstructure of the gels and therefore the final product can be controlled. As a result of hydrolysis and condensation reactions, clusters grow and bond and form a gel. Since the size and shape of the final product are determined during the gelling stage, this stage must be well controlled. The gelation time is one of the critical parameters of the process to obtain low density and porous products. It is known that the density of particles increases with increasing gelation time. It is stated in the literature that the gelation time is long even when the pH value of the sol is low. Since gelation occurs through hydrolysis and condensation reactions, it is directly affected by every parameter that affects these reactions. The resulting gel material contains hydroxyl and organic residues. These residues must be destroyed to prepare a true inorganic structure. To destroy the formed pores, when the volatile substances in the pore are removed, the gel begins to swell and this causes the structure of the gel to deteriorate (Dilsiz & Akovali, 2002; Thitinun et al., 2003).

The sol-gel process has many advantages when compared to other powder production methods. These advantages are given below:

- The temperatures needed in all steps, except the condensation, are low and often close to room temperature. Thus, the risk of thermal degradation of the material is minimized and high purity, and stoichiometry can be obtained.
- Preliminary starting materials such as metal alkoxides and mixed alkyl/alkoxides are mostly volatile. This ensures a high purity of the product.
- The chemical conditions of the process are moderate. Hydrolysis and condensation are catalyzed by acids and bases. With certain methods, organic structures with pH sensitivity and even biological species containing enzymes and all cells can be retained and still be able to continue their functions.
- High porosity materials and nanocrystalline materials can be prepared with this process.

- By controlling the aging and drying conditions, pore size, and mechanical strength can also be controlled.
- Since the liquid precursors are used, it is possible to cast ceramic materials into various complex shapes and produce fibers or thin films without the need for processing or melting.
- The low temperature of the sol-gel process is often below the crystallization temperature of oxide materials, allowing the production of rare amorphous material of this product (Brinker & Scherer, 2013; Ün, 2008).

2.5.3 Compaction

Compaction is the process of applying pressure utilizing upper and lower punches in a suitable mold to bring the powders into the desired shape. With the compaction process, the piece gains a certain strength. This pressed piece is called a green compact. Meanwhile, the green compact formed by the cold fusion of the powder grains in the mass maintains its shape. While the green compact is being taken out of the mold and taken into the furnace before sintering, it must have a certain strength. The final shape and mechanical properties are directly related to the green compact density level and homogeneity. Powders under the press do not behave like a liquid, the pressure is not homogeneously transmitted to the whole structure, and a very small amount of powder flows along the mold wall. For this reason, the density of the effective green part depends on the mold and equipment design.

Theoretically, it is estimated that each particle is in contact with neighbors in the first stage. Meanwhile, no bonding has yet occurred between the powders. As seen in Figure 2.11, as pressure is applied, the particles settle into the mold, change shape and mechanical bonding occurs. The density after compression is called raw density, and the strength after compression is called raw strength. Since deformation increases the hardness of the parts, higher pressure must be applied to continue pressing (Sarıtaş et al., 2007).

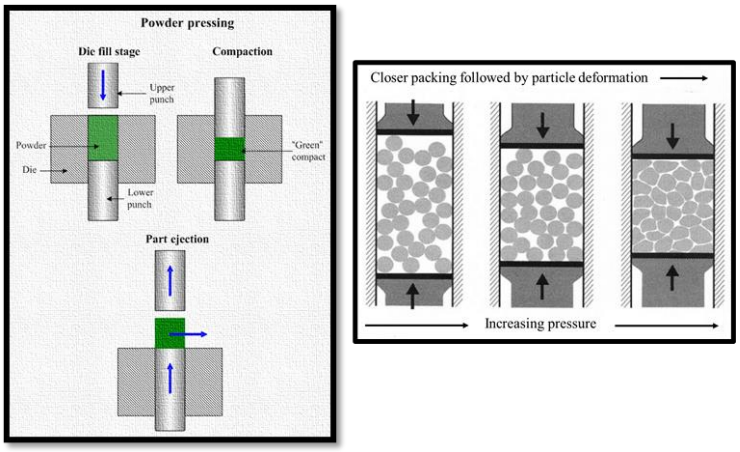

Figure 2.11 Demonstration of single-axis pressing method and an overview of the powder compression stages

All applied compacting methods are divided into two main groups as hot and cold compaction. Compaction methods, which are isostatic (hot), extrusion, die compacting, spraying, and pressureless sintering are included in the hot compaction group while die compacting, isostatic (cold), rolling injection molding, slip casting, and slurry casting are in the cold compaction group. Isostatic pressing is a PM forming process that exerts even pressure on a powder compact in all directions, thus providing a better density and microstructure homogeneity without the geometric constraints of the uniaxial pressing as seen in Figure 2.12.

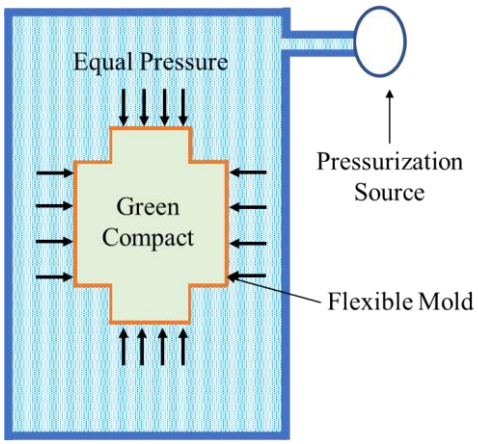

Figure 2.12 A model demonstrates the CIP process

Isostatic pressing has two different methods as "cold" or "hot". Cold isostatic pressing (CIP) is used to compress green parts at ambient temperatures, while hot isostatic pressing (HIP) fully joins parts at high temperatures through solid-state diffusion. In other words, while it is necessary to apply the sintering process to products after CIP, this process is not required for HIP (Kuşoğlu, 2011).

2.5.4 Sintering

Sintering is the process of keeping the green parts at a certain temperature for a certain time under a controlled atmosphere and ensuring that the particles in contact with each other are bound together by diffusion at high temperatures. Sintering is realized at a temperature of about 0.4-0.9 of the absolute melting point of the materials. The sintering process is a heat treatment process that allows material transport to reduce the specific surface area of porous powders with raw strength and to reduce the pore volume by enlarging the contact areas of the powders. The bonding of particles realized by the diffusion of atoms brings integrity to the compact structure. Besides, shrinkage carries out during the sintering resulting in the densification of the part. As a result of the sintering process, densification and strength increase occurs in the green compact.

Surface energy per unit volume is inversely proportional to particle size. Therefore, smaller particles with a higher specific surface area have higher energy. In this way, the sintering process of small particles takes place in a shorter time. Of course, not all of the surface energy is devoted to sintering. Almost all particle contact surfaces in crystalline solids create grain boundaries. As a result, neck growth decreases surface energy while increasing grain boundary energy (German, 2005; Güler, 2016).

The sintering process is divided into two different groups as solid-state and liquid phase sintering. Also, spark sintering, microwave sintering, and laser sintering are various methods used in specific applications. Solid-state sintering involves material transport by diffusion. The driving force required for this process is the free energy or chemical potential difference between the neck area and the surface of the powder.

Transport of the material in solid-state sintering is shown schematically in Figure 2.13. The neck region is the source for atomic voids and the migration zone at the surfaces of powders. In liquid phase sintering, one of the phases is in a viscous state at the sintering temperature. This is especially seen in sintering materials with very different melting points. The liquid phase wets the solid powders and high capillary pressure occurs in the fine channels between the powders. In fine powders, the amount of capillary pressure is higher and sintering becomes easier. Liquid-phase sintering is widely applied in silicate systems (Güler, 2016).

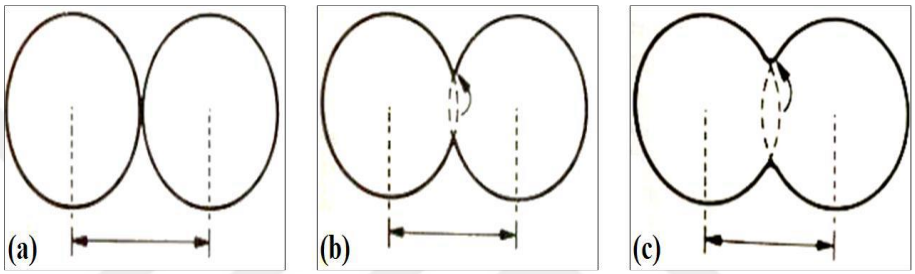

Figure 2.13 Material transport in solid-state sintering; (a) particles in contact, (b) neck formation by inter-particle diffusion, (c) coalescence of particles

As can be seen in Figure 2.14, there are contact points between the powders compressed in the initial state. At this state, larger pores occur between small grains. With the sintering process, the bonds between particles expand and neck formation begins. Thus, the grain size increases, the pore size decreases. Instead of the solid-vapor interface, one boundary grows at the contact points. In the last stage of the sintering process, two particles are completely combined to form a single grain.

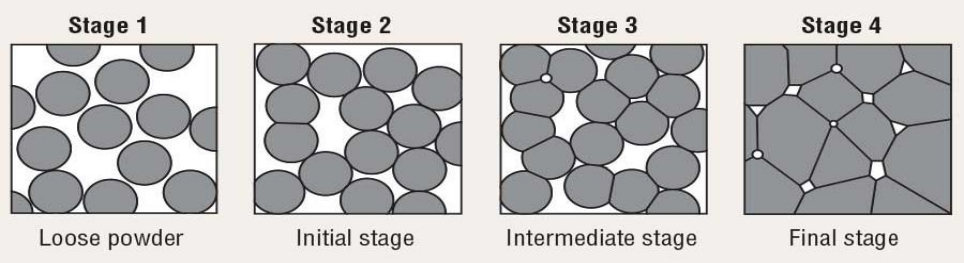

Figure 2.14 A model explaining the sintering process (Aytimur et al., 2014)

CHAPTER THREE
LITERATURE REVIEW

3.1 Nickel Oxide (NiO_x)

Nickel oxide (NiO) is a well known intrinsic p-type semiconductor and categorized as a binary transition metal oxide. NiO has a wide bandgap in the range of 3.6 – 4.0 eV. NiO shows antiferromagnetic properties below the 250 °C Neel temperature. The melting point of NiO is 1955 °C and a density is 6.67g/cm^3 (Khan, 2016). NiO has superior properties like as great thermal and chemical stabilities, good optical transparency, etc. The NiO has simple and various production methods such as solution and vapor-based techniques (Etgar, 2016; Yin et al., 2016).

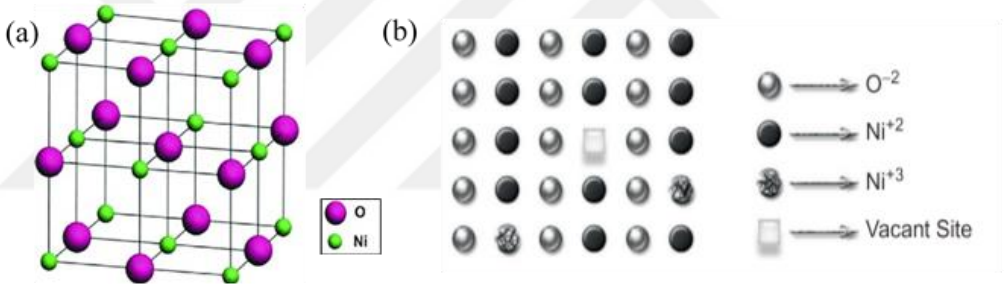

Figure 3.1 (a) The crystal structure of NiO as a unit cell (green color represents Ni atoms, purple color represents O atoms), (b) schematic diagram showing cation vacancies trapping positive holes (p) in nonstoichiometric NiO (Nandy et al., 2007)

Moreover, NiO has a rock salt crystalline structure (space group: Fm3m), also called both cubic and/or NaCl type structure, with nickel vacancies (Ni^{2+}) and interstitial oxygen (O^{2-}) sites (Figure 3.1). These microstructural defects can occur during the different production methods and cause the crystal structure to be non-stoichiometric (NiO_x) (Dirksen, Duval, & Ring, 2001). In high-temperature production, nickel oxide generally takes in excess of oxygen, which causes the oxidation of Ni^{2+} to Ni^{3+} simultaneously, so that nickel voids and intermediate oxygen are formed in the crystal. Nickel oxide shows p-type semiconductor properties due to the excess of oxygen formed as a result of oxidation (Suman et al., 2007). Nickel

vacancies are formed in the nickel cation regions in the NiO structure due to excess of oxygen atoms and can be ionized to form Ni^{3+} ions. This reaction demonstrates with Kröger-Vink notation as below:

$$2Ni_{Ni}^{X} + \frac{1}{2} O_2(g) \rightarrow 2Ni_{Ni}^{\bullet} + O_O^X + V_{Ni}^{''}\bullet \quad (3.1)$$

The two Ni^{2+} ions (Ni_{Ni}^{X}) react with oxygen, producing an ionized nickel vacancy ($V_{Ni}^{''}\bullet$) and two Ni^{3+} ions ($Ni_{Ni}^{\bullet}$) in the NiO crystal. The created Ni^{3+} ions function as acceptors which donate a hole and also affect the conductivity of NiO_x film (Oflaz, 2019).

The NiO properties of such electrical, optical, mechanical differ depending on whether it is stoichiometric or not. For example, in the $Ni_{1-x}O$ structure, when x takes a value between 0 and 0.005, at the x point near the upper limit, the color of NiO is black/brownish while at a smaller x value the color is green. An ideal stoichiometric NiO acts as an insulator when there are no defects in its structure and the conductivity and resistivity of ideal NiO is 10^{-4} S/cm and 10^{6}-10^{13} Ω.cm, respectively (Khan, 2016). It is seen in studies in the literature that the electrical conductivity of nickel oxide is directly related to these defects (Antoini, 1992).

3.2 Lithium Doped NiO_x HTMs

In NiO_x films, the conduction mechanism is provided by holes. These holes are generated from Ni^{+2} vacancies, oxygen interstitials, and additives (dopants). Doping of NiO_x with metallic ions alters the electrical properties as well as the transmittance, morphology, charge extraction and, energy level alignment. Accordingly, the ionic doping in NiO_x crystal lattice can create crystal lattice distortion and defects which may lead to the degradation of carrier mobility and recombination. However, considering the property changes with the incorporation of various metals into the NiO_x substrate, a lot of effort has been put into this area and very promising

improvements have been made in the performance of NiO_x-based PSCs. More generally, investigating the effect of the contribution of inorganic HTMs on PCEs in PSCs is considered as an important aspect of performance optimization. A diagram summarizing the effects of different doping strategies on the properties of NiO_x HTMs is given in Figure 3.2.

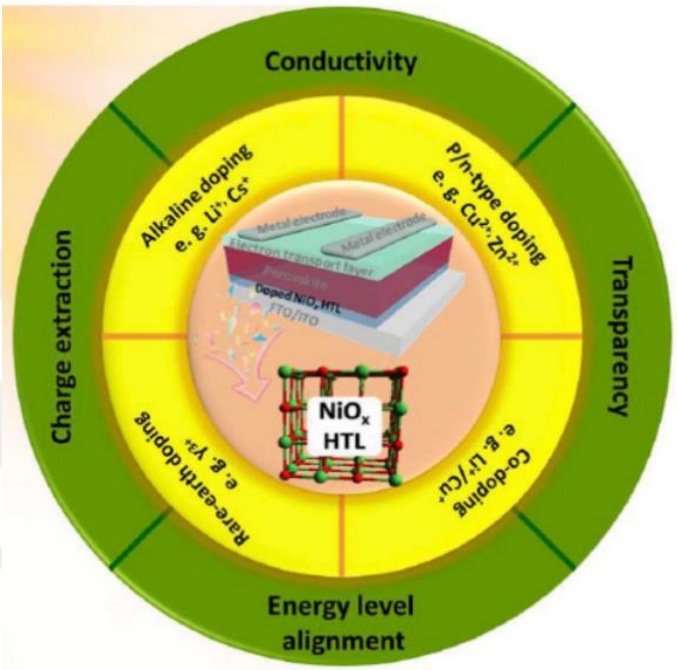

Figure 3.2 Schematic diagram summarizing the different types of doping discussed in this review and their influence on the properties of NiO_x HTMs (Xu et al., 2019)

For the doping effect to be significant, an additive element similar to the Ni^{2+} ion radius should be used, which increases the lattice stability and reduces the mismatch. In addition, the additive element should increase the relative content of Ni^{3+} acceptors. When these conditions are considered, elements such as Cu, Li, Mg, Cs, and Au are being used as additives since they have these properties.

The ionic radius of Lithium-ion (Li^+) (0.76 Å) is similar to the ionic radius of Ni^{2+} (0.69 Å). The large atomic radius of the Li-ion results in the formation of a shallower level of acceptor in NiO_x under Ni-poor and O-rich conditions, making it a suitable acceptor additive and can be effectively incorporated into the NiO_x lattice.

Nevertheless, p-type metal ion doping including monovalent alkali metals such as Li^+ can increase the electrical conductivity of the NiO_x films.

3.3 Literature on NiO_x and Li:NiO_x

In this section, literature review of each step aimed in the thesis study is included. These are the production of NiO-based powder, target material production from the obtained powders, and then producing NiO_x HTMs for use in PSCs using the sputtering method from the target materials. To the best of our knowledge, the studies that have been carried out to date have been explained in detail in Table 3.1.

NiO_x films were first used as HTM in n-i-p structured PSC as an alternative to PEDOT:PSS and achieved improved stability and reduced hysteresis (Irwin, et al., 2008). In a study reported in 2014, NiO_x was used as HTM in the PSC device in p-i-n architecture with Glass/ITO/NiO_x/$CH_3NH_3PbI_3$/PCBM/BCP/Al configuration, and an efficiency of up to 7.8% was obtained (Jeng et al., 2014).

Later, it was used as HTM in PSCs as it has better effects on hole removal and long term stability than other inorganics. In n-i-p structure, NiO_x HTM, produced by many solution techniques such as spin coating, screen printing, was used in solar cells and its effects were investigated. It is difficult to deposit NiO_x directly on the perovskite layer because the solvent used in the precursor solution for NiO_x soluble is strongly polar organic or water. In a study using sputter-deposited NiO_x / Ni double layer as an HTM / contact pair in the normal architecture of a perovskite solar cell; It has been reported that the solar cell's efficiency increased from 1.3% to 7.28% within 6 days, resulting in durable perovskite solar cells for more than 60 days. Deposition of this layer by dc reactive magnetron sputtering enabled the perovskite layer to have a smooth and crack-free film without any negative effect on the surface protection against moisture and oxygen and the perovskite structure (Nejand, et al., 2015).

Table 3.1 List of the device performances of NiOx based hole transport materials

HTM	Device Configuration	Production Method	PCE (%)	Ref.
NiO_x	ITO/NiO/meso-NiO/$MAPbI_3$/PCBM/BCP/Al	Magnetron Sputtering	11.60	(Wang et al., 2014)
NiO_x	ITO/NiO_X/$CH_3NH_3PbI_3$/PCBM/BCP/Al	Spin coating	7.8	(Jeng et al., 2014)
NiO_x	FTO/NiO/$MAPbI_{3-x}Cl_x$/PCBM/Ag	Electrodeposition	7.25	(Subbiah et al., 2014)
NiO_x	FTO/NiO/meso-Al_2O_3/$MAPbI_3$/PCBM/BCP/Ag	Spray Pyrolysis	13.49	(Chen et al., 2015)
NiO_x	ITO/PLD-NiO/$MAPbI_3$/PCBM/LiF/Al	Pulsed Laser Deposition	17.30	(Park et al., 2015)
NiO_x	ITO/NiO_x/$MAPbI_3$/PCBM/BCP/Ag	Electron Beam Evaporation	15.40	(Pae et al., 2018)
Li: NiO_x	ITO/Li:NiO_x/$MAPbI_3$/PCBM/Ag	Spin Coating	15.41	(Park et al., 2018)
Li: NiO_x	ITO/Li:NiO_x/$MAPbI_{3-x}Cl_x$/PCBM/Al	Spin Coating	18.00	(Nie et al., 2018)
Li: NiO_x	ITO/Li:NiOx/$[(FAPbI_3)_{0.85}(MAPbBr_3)_{0.15}]_{0.95}(CsPbI_3)_{0.05}$/PCBM/BCP/Ag	Spin Coating	17.34	(Guo et al., 2020)

Park and his team produced Li-doped NiO_x films by adding different amounts of lithium to the NiO_x solution and examined the performance of these HTMs in PSC. As a result of the study, it has been proven that the permeability spectra do not show a significant change even with the addition of 15% Li (at %). In addition, the highest efficiency in the study was the NiO_x HTM cell with 5% Li (at %) doped, and it was measured as 15.41% (Park et al., 2018).

Guo et. al have studied the effects of energy level alignment of NiO_x on carrier transfer and recombination dynamics. They reported that Li doping shifts down the valence band of NiO_x significantly and that Li additive content of 4% is in optimum energy level harmony with NiOx and perovskite and cell efficiency was measured as 17.34% (Guo et al., 2020).

Among other types, the inverted planar structure is of increasing interest due to its simplicity, the possibility of low operating temperature, and especially negligible hysteresis effects. Unlike the normal planar structure, liquid phase and gas phase deposition methods are frequently used. Among these, PVD, which is a gas phase deposition method; provides controllable morphology, composition, thickness, and surface properties, so that they are superior to other deposition methods. However, generally, a target material is required for deposition. Therefore, many studies have a target making stage for the sputtering system. The size, density, and chemistry of the target material change the thin film deposition parameters, so they are important criteria. Basically, target material production includes the application of a sintering process to increase the density after raw shaping with the help of a hydraulic, cold isostatic press.

In a study carried out for this purpose, high purity NiO powders (> 99.9%, Aldrich Co.) were used to make a target material with a diameter of 50 mm, and a sintering process was applied at 1350 °C for 3 hours. Then it was used in the RF scattering method and the effect of sputtering gas ratios (Ar and O) on film crystallographic properties was investigated. The (100) oriented NiO film with good crystallinity was obtained in an Ar atmosphere and while obtaining the oriented film in an O_2 atmosphere (111), the film was reported not to crystallize in the Ar-O_2 mixed gas (50% Ar + 50% O_2). (Ryu et al., 2004).

In another study, the target material produced for the sputtering method was made with commercially available NiO powder (99.99% pure). Polycrystalline NiO powder was pressed into pellets with a hydrostatic pressure of 200 kgf/cm^2 with polyvinyl alcohol (5%) as a binder. Two-stage heat treatment was applied to the pellets. It was first sintered in a furnace at 150 °C for 12 hours, then raised upto 450 °C and held at this temperature for 10 hours to remove the carbon from the target material, and the resulting target materials were 50.8 mm in diameter and 6.35 mm in thickness. Ultra-smooth NiO thin films were deposited on PET and glass substrates at a low substrate temperature and a low deposition pressure using RF magnetron sputtering. Low temperature deposited films of ultra-smooth NiO thin films on PET substrate have been reported for the first time and this study is important for flexible semiconductor device technology (Nandy et al., 2010).

In addition to neat NiO target materials, doped target materials were also produced. Chang and his teams who conducted such a study; lithium carbonate (Sigma-Aldrich, 98%, Li_2CO_3) powders in various amounts between 0-15% by weight were mixed with high purity NiO powders in separate experiments, then the mixed powders were heat-treated at 900 °C for 24 hours. After grinding, the resulting LiNiO powders were filled into a mold and pressed to obtain a pellet of 50.8 mm of diameter and 10 mm of thickness. The pellet was then, sintered at 1100 °C for 24 hours to achieve the desired targets. In this study, electrochromic LiNiO films were deposited on ITO substrates using RF magnetron sputtering technology at room temperature. Cyclic voltammetry analysis of electrochromic films has reported that CV's hysteresis field increases as Li^+ ions are incorporated into NiO and has proven to be suitable for applications such as smart windows (Chang et al., 2020).

In addition to these target material studies, in a part of Par Park's thesis, it was reported that neat and Li doped NiO target pellets were produced for the PLD system and that the undoped and Li doped thin films were successfully grown. Stoichiometric $Ni^{II}O$ powder (green color) was pressed under 200 kg /cm^2 pressure with a typical hand pressing machine and then annealed at 800 °C for 24 hours under atmospheric conditions. The surface of the target material obtained after heat treatment was removed with a piece of sandpaper. The target material retained its original green color after sintering at 800 °C. This has proven that nickel ions remain stabilized as Ni^{2+}. For LiNiO target materials, Li_2CO_3 and NiO powder mixture was heat-treated at 650 °C for 10 hours. Later, the powder was ground and pelleted and sintered under the same conditions as the NiO pellet. LiNiO target material is black in contrast to the pristine NiO. This color explains the presence of Ni^{3+}, as one would reasonably expect from LiNiO composition. The density of NiO and LiNiO target materials is 4.43 and 4.56 g/cm^3, respectively (65% to 83% of the theoretical density). It has been shown that the denser LiNiO target material compared to NiO is associated with the presence of lithium that promotes grain percolation (Par Park, 2010).

When the above studies were examined, it was seen that these NiOx thin films were obtained by many different methods such as solution-based and steam-based. Solution-based thin-film production methods have good properties such as good stoichiometry control, easy application, low-cost precursors, and low-cost equipment. Thin films

coated by steam-based methods have better properties than solution-based thin film, such as good surface roughness, good mechanical properties, high homogeneity. However, there are disadvantages such as expensive equipment and the need for costly materials such as target material. Therefore, the purpose and originality of the thesis work; Production of target material from powders obtained by sol-gel method is advantageous for many reasons. Because there are some difficulties in commercially sold target materials. These can be listed as follows:

- Many thin films can be coated with a single target material.
- Metal oxide target materials are sold at high prices depending on their quality.
- Suitable stoichiometry target materials made from the desired additive elements are not commercially available.

CHAPTER FOUR
EXPERIMENTAL METHODS

4.1 Purpose

As stated in the previous sections, the NiO_x layers as the hole transport materials of perovskite solar cells are usually deposited through RF magnetron sputtering systems in which commercial NiO_x targets are employed (Chen, et al., 2005; Jamal et al., 2019; Lee et al., 2007; Usha et al., 2016). In this thesis, several RF magnetron sputtering targets with different structural and chemical configurations were produced to evaluate their suitability and performances on the thin film deposition process. To produce the targets; sol-gel derived pristine NiOx and Li doped NiO_x powders and commercial NiO_x powders were used. The commercial, pristine, and Li doped NiO_x powders mixed with binders were then performed by a hydraulic press. The final target geometry and dimensions were obtained after sequentially applied cold isostatic pressing and sintering. Both the CIP process with high pressure and the sintering process with high-temperature were applied to the target materials for removing porosities and to make them denser which are important criteria of magnetron sputtering targets (Liu et al., 2011; Neves et al., 2012; Sumıtomo Electrıc Industrıes, Ltd ., 2020).To scrutinize the performance of the produced sputtering targets, film depositions were performed under suitable conditions. Finally, the intermediate products; powders, targets, and thin films of each configuration were elaborately evaluated by critical physical, structural, morphological, optical, and electrical characterization methods.

4.2 Materials

In this part, the chemicals used in the production of sol-gel based pristine and Li doped NiO_x nanopowders are listed. The materials were shown with their name, chemical formula, purities, CAS number, and, the suppliers in Table 4.1.

It is important to note that all chemicals were used without any further purification. Additionally, to provide a practical sample designation; commercial NiO_x, pristine NiO_x and, Li doped NiO_x are identified as "**C-NiO**", "**P-NiO**", and "**Li-NiO**".

Table 4.1 Table of the chemicals used in the production of pristine and Li doped nanopowders

Materials	Purity	CAS Number	Supplier
Nickel Nitrate Hexahydrate ($Ni(NO_3)_2.6H_2O$)	≥ 97%	13478-00-7	Sigma Aldrich
Lithium Nitrate ($LiNO_3$)	≥ 98%	7790-69-4	Sigma Aldrich
Methanol (CH_3OH)	≥ 99.8% (ACS Reagent)	67-56-1	Sigma Aldrich
Acetic Acid (Glacial) (CH_3CO_2H)	≥ 99.7% (ACS Reagent)	64-19-7	Sigma Aldrich
Commercial NiO powder (NiO)	NA	NA	REFSAN
Polyvinyl alcohol (PVA) $((C_2H_4O)_x)$	≥ 99% hydrolyzed	9002-89-5	Sigma Aldrich

4.3 Methods

The experimental studies conducted in this thesis were depicted in Figure 4.1.; the flow chart for the production of powders, target materials, and thin films. Pristine and Li-doped powders were produced through the sol-gel method. Homogeneous solutions were obtained using the solvents (methanol) and precursors (nickel nitrate hexahydrate, lithium nitrate). The solutions were kept on a hot plate to complete the gelation step, and then the dried gel was ground by hand in a mortar. Heat treatment was applied to remove organic residuals and to obtain crystalline powders.

Then, C-NiO, P-NiO and, Li-NiO powders were compacted in pellet form by a hydraulic press. The CIP process with high pressure and the sintering process with high-temperature were applied to the pellets for removing porosities and to make them denser. These pellets were used as target material in the RF magnetron sputtering system to deposit NiO_x thin film on the glass substrate, and with this production, the experimental section was completed.

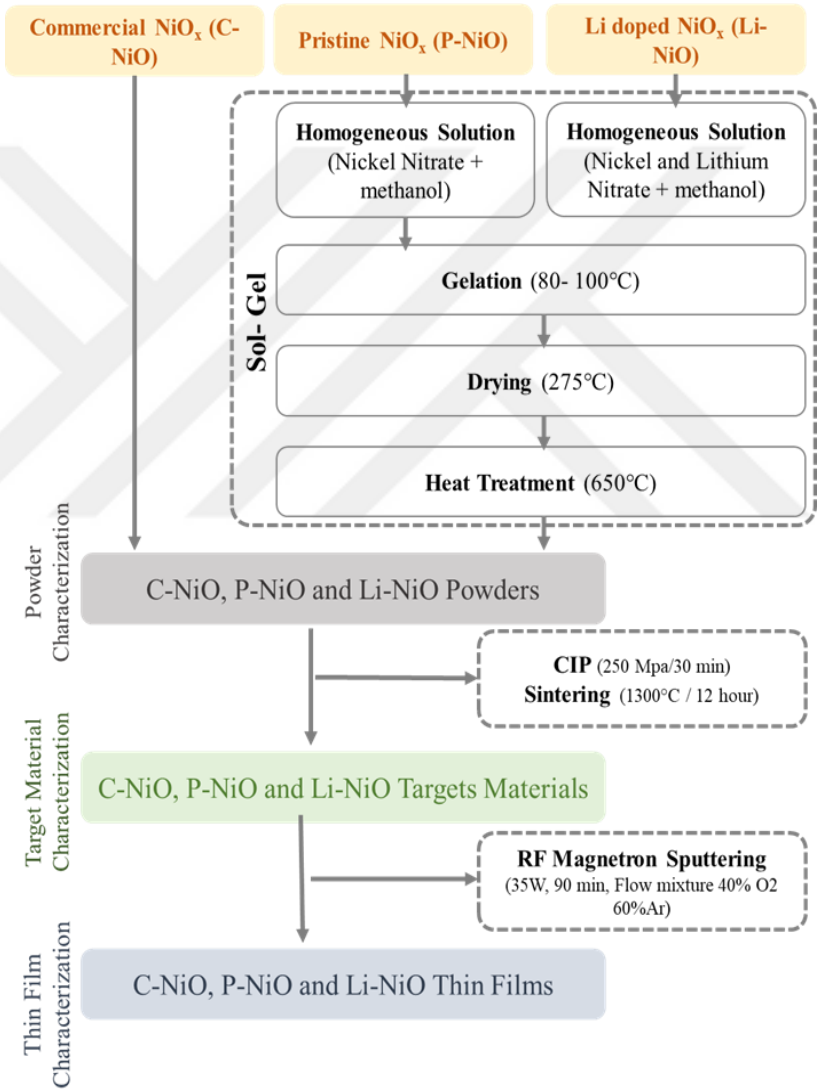

Figure 4.1 The flowchart of production steps of the thesis

The solution was prepared by dissolving 44.96 g nickel nitrate hexahydrate in 100 mL methanol for **P-NiO**, and 42.72 g nickel nitrate hexahydrate and 0.52 g lithium nitrate in 100 mL methanol for **Li-NiO** with the addition of acetic acid for arranged pH value to ≈ 2 (WTW, pH 3110 Set 2) and the homogeneity of the prepared transparent solution was measured with a turbidity meter (Velp Scientifica, TB1), with a value of ≤ 1.5 ntu (nephelometric turbidity unit) (Figure 4.2.a). The solution was then kept at 80-100 °C after stirring for 60 minutes until it becomes gel form (Figure 4.2.b,c). After gelation, the **P-NiO** and **Li-NiO** powders were ground in a mortar (Figure 4.2.d). The powders obtained were dried at 275 °C for 2 hours to remove the residual organics and hydroxyl group from the structure and then, heat-treatment was applied at 650 °C for 2 hours to the powders (Figure 4.2.e). The powder amount obtained at the end of the sol-gel method was ≈ 20 g, and as a result of the heat treatment, the color of the P-NiO powder changed from green to grayish and, the color of the Li-NiO powder changed from green to black.

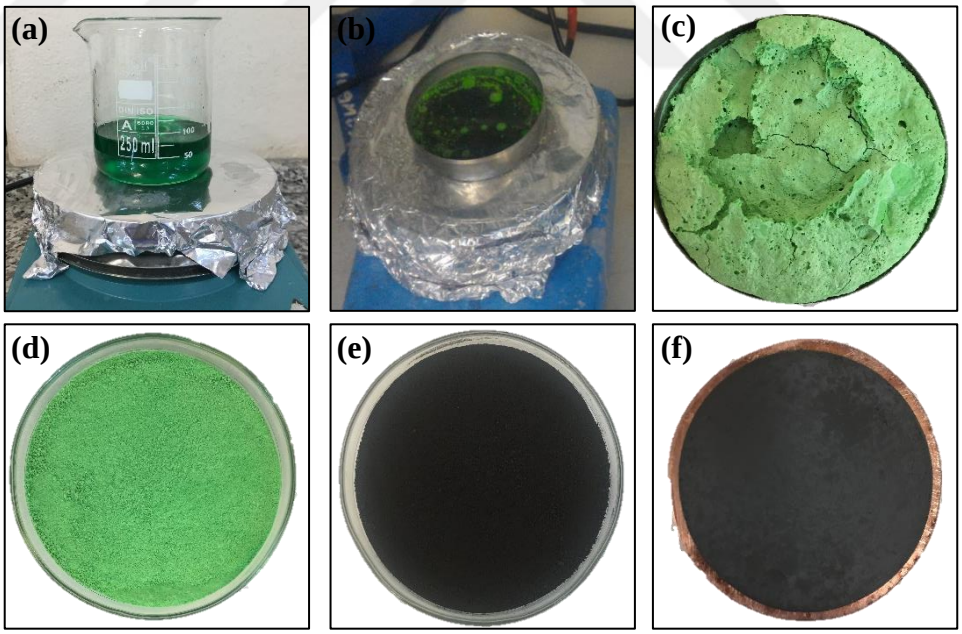

Figure 4.2 Demonstration of a sol-gel method to obtain powder from the solution: (e) and (f) images belong to Li-NiO (Personal archive, 2020)

The hydraulic press was used to perform in all of the target material production. Powders used for the production of target material were mixed with PVA binder (3% by weight). This step was aimed to coat the powders homogeneously with the binder. These mixtures were dried at 150° for 1 hour, then placed in a 2-inch diameter mold and kept for 5 minutes under 0.1 MPa (10 tons/m^2) of a manual hydraulic press (Specac, Atlas). The target materials were put into the plastic bag and the air inside of the bag was vacuumed. Then, vacuumed samples were placed in the CIP (AIP, CP360) device for 30 minutes under 250 MPa (25000 tons/m^2) pressure for decreasing porosities amount and the size. Then, heat treatment was applied to perform the sintering process of the target materials. The heating regime and time for important parameters for sintering. In this thesis, the furnace temperature was raised from room temperature to 600 °C at 2.5 °C/min, from 600 °C to 1300 °C at 5 °C/min (Protherm PLF 130/6). Targets were sintered at 1300 °C for 12 hours and left to cool to the room temperature after sintering was finished (Figure 4.3) (Liu et al., 2020).

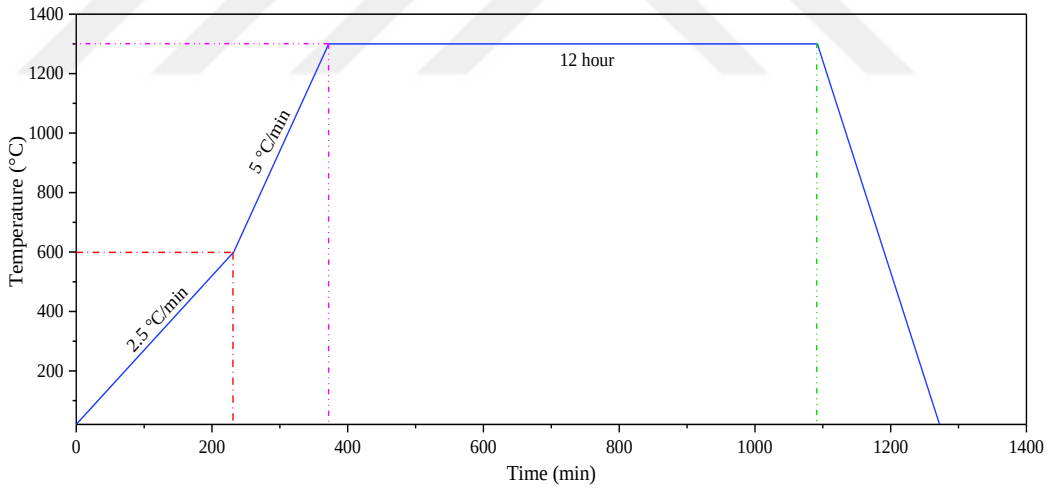

Figure 4.3 Graph of heat treatment regime applied to all NiO_x pellets

The obtained target materials were used in the magnetron sputter system for deposition NiO_x based thin film. Before placed into the chamber, the substrates (glass / ITO) were cleaned with ethanol and deionized water by standard process. NiO_x based targets were pre-sputtered for 15 min for removing the impurities. The chamber was

evacuated to a base pressure of ≤ $4x10^{-4}$ Pa before introducing the sputtering Ar and O_2 gas mixtures. All the deposition conditions like temperature, flow rates, time, and chamber gas pressure were maintained constant for all the deposition sets. The details of the deposition parameters have been shown in Table 4.2.

Table 4.2. RF Sputtering parameters and conditions

RF Power	35 W (C-NiO) 45W (P-NiO / Li-NiO)
Base Vacuum	3- 4.5 x 10^{-6} Torr
Deposition Pressure	4 x 10^{-2} Torr
Sputtering Time	90 min
Gas Flow Ratio	40% O_2 / 60% Ar [O_2 / (Ar + O_2)] : 40%
Type of Substrate Used	ITO/Glass
The substrate to Target Distance	10 cm
Substrate Temperature	Room Temperature
Target Diameters	39 mm (C-NiO) 45 mm (P-NiO / Li-NiO)

4.4 Materials Characterization

4.4.1 X-Ray Diffraction (XRD)

The XRD measurements were performed to determine the crystal structure of NiO_x in different forms like powder, target materials, and thin-films and to examine the crystal structure changes with Li doping. The XRD (Thermo Scientific, ARL X'TRA) system was used with Cu-Kα (1.54185 Å) radiation and, at last, diffraction patterns were obtained between diffraction angles (2θ) of 10°-90° at room temperature with a scan rate of 4°/min for NiO_x nanopowder and target materials. The NiO_x thin films were scanned with thin-film mode between 10°-90° diffraction angles at a scan rate of 2°/min.

4.4.2 Scanning Electron Spectroscopy (SEM)

The SEM (Zeiss, Gemini) system, was used to examine the surface morphology of powder, target material, and thin films using secondary electrons (SE) at 5 kV voltage, and to perform elemental analysis of the samples. The magnifications used for analysis were 1K, 5K, 10K, 20K, and 50K.

4.4.3 X-Ray Photoelectron Spectroscopy (XPS)

The XPS is the measurement of photoelectrons ejected from the surface of a material irradiated with X rays. It gives information about elemental composition, empirical formula, chemical state, and electronic state of the elements that exist within a material. The XPS (Thermo Scientific, K-Alpha) system uses Al-Kα source gun type and requires ultra-high vacuum conditions. The XPS data of the survey scan was acquired from 0 to 1400 eV with a scanning rate of 1 eV utilizing pass energy of 150 eV. The scanning for each sample was performed 15 times from a single point. The data of the elemental scan occurred with a scanning rate of 0.1 eV utilizing pass energy of 30 eV. The scanning for each sample was performed 10 times from a single point.

4.4.4 Particle Size Distribution (PDS)

This characterization uses to measure particle and molecular size of the sample with a dynamic light scattering technique (Malvern, Zeta Sizer Nano ZS90). For measurement, powders are dispersed in non-dissolving liquids, light beams from the source pass around the particles, the size of the particle is calculated by the light beams collected in the detector.

4.4.5 Determination of Density

In almost all ceramic systems, the density of the materials is of great importance, especially in high strength or high-temperature applications. In principle, the volume of pores in a sample is calculated from the weight of the water required to fill them. Since this method is based on Archimedes' Principle, it is also called Archimedes Method. The two formulas shown below are important for determining the density of ceramic materials Ceramic samples are dried in the oven until their weight remains constant and the weight of the samples are measured on a precision scale. The samples are then thrown into boiling water, boiling continues for 4 hours, then cooling down to room temperature. The samples are weighed by their suspended weight in water in a specially prepared device for the experiment. Then the sample is take outed from the water, the water on its surface is wiped and quickly weighed on the balance.

- Bulk Density: It is calculated as the ratio of sample weight to bulk volume. The bulk volume includes powder volume, inter-particle space volume, and closed and open-pore volume.
- Apparent Solid Density: Calculated as the ratio of sample weight to apparent solid volume. The visible volume includes the volume of powder and the volume of closed pores.

$$\text{Bulk Density} = \frac{specimen\ mass}{bulk\ volume} = \frac{W_K}{W_D - W_A}\ x\ \rho_{\text{water}} \qquad (4.2)$$

$$\text{Apparent Solid Density} = \frac{specimen\ mass}{apperent\ solid\ volume} = \frac{W_K}{W_K - W_A}\ x\ \rho_{water} \qquad (4.3)$$

W_K = weight of dry sintered sample in the air (g)

W_A = suspended weight of the water-impregnated sample in water (g)

W_D = weight of sample impregnated with water in the air (g)

ρ_{liquid} = density of the water

CHAPTER FIVE
RESULT AND DISCUSSION

This thesis covers the characterization of three subsections of the sequential interproducts as powders, targets, and thin films. Obtained results and the discussions were organized depending on this order. Initially, the detailed evaluation of the powders was given. The targets produced using the powders were handled as the second interproduct. Finally, thin-films growth using the optimal powders and targets were scrutinized through a deep characterization.

5.1 Characterization of Powder

5.1.1 Structural Properties

The crystal structure of the C-NiO, P-NiO, and Li-NiO powders were determined via X-ray diffractometer as given in Figure 5.1. Here it is important to note that, the sol-gel derived P-NiO and Li-NiO powders were heat-treated at 650 °C for 2 hours but C-NiO, commercially purchased, was used as received. Therefore, P-NiO and Li-NiO peaks, especially the main characteristic peak at 43°, are narrowly wide and sharper, compared to C-NiO peaks which can be attributed to its less crystalline structure with smaller grain size (Liu et al., 2017) The characteristic XRD peaks around 37°, 43°, 62°, 76°, and 79° show the presence of cubic nickel oxide with space group Fm3m phase due to (111), (200), (220), (311), and (222) lattice plane, respectively. No peaks from lithium compounds or the impurity phases can be observed, suggesting that the lithium doping does not change the original NiO structure. All patterns are in good agreement with the JCPDS card no. 04-0835 (Wei et al., 2009). The X-ray diffraction patterns of NiO_x based powders in the 2θ range of 42° to 45° are also shown on the right side of Figure 5.1. The position of the C-NiO peaks is noticed to shift slightly towards higher angles by around 0.34° than P-NiO peaks. This suggests that due to Li^+ doping, the lattice constant of NiO crystal reduced (Li et al., 2016).

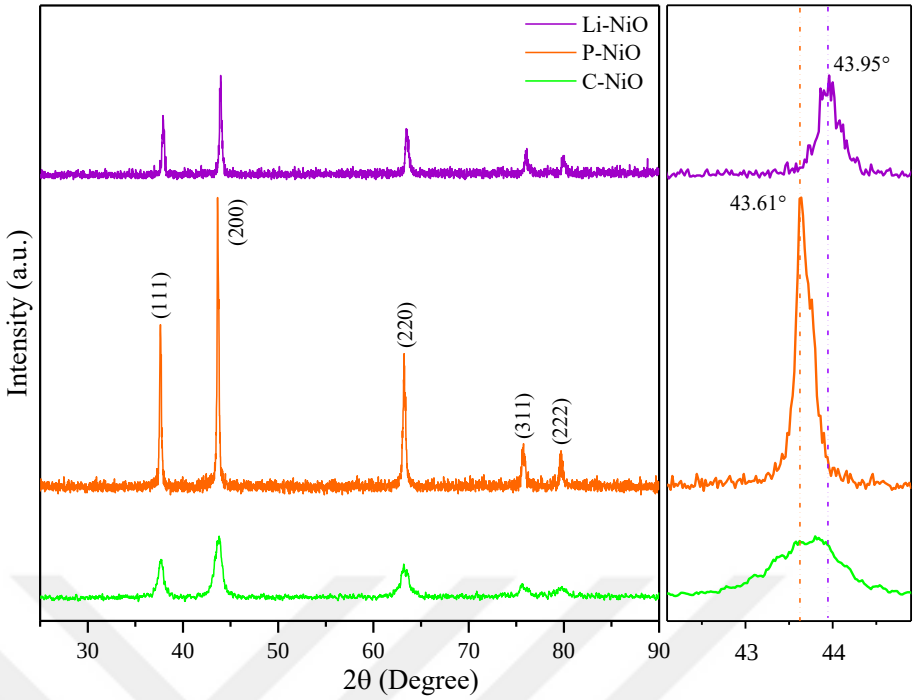

Figure 5.1 XRD models of C-NiO, P-NiO, and Li-NiO powders between 25 and 90° are given. On the right side of the graph, the characteristic peak is shifted in the graph limited to 42-45°region

According to the results of XRD analysis, the crystallite sizes of C-NiO, P-NiO, and Li-NiO powders were calculated using the Debye-Scherer equation (Danial et al., 2015).

$$D = \frac{K\lambda}{\beta cos\theta} \tag{5.1}$$

where; D is the mean crystallite size of the powder, K is a constant shape factor equal to 0.89, λ is 0.15406 nm is the wavelength of CuK_α, β is the Full Width at Half Maximum (FWHM) intensity of 2θ x (π/180), and θ is Brasgg's diffraction angle.

The average crystallite size of C-NiO, P-NiO, and Li-NiO was calculated to be 7.52, 27.45, and 22.81 nm, respectively as presented in Table 5.1. The results obtained show that the crystal size decreases with Li entering into the NiO_x structure. The results obtained are consistent with the study in which Zhang et al. Measured the lattice constant with a similar approach (Zhang et al., 2018). Since Li^+ (0.76 Å) has a similar ionic radius as Ni^{2+}(0.69 Å), it can be effectively doped into the NiOx lattice. The

continuous lattice parameter reduction with increasing Li^+ dopant concentration can be attributed to the substitutional sites being occupied by the Li^+ ions (Dutta et al., 2010).

Table 5.1 Crystallite size calculation of C-NiO, P-Nio, and Li-NiO powders (2 Theta refers to peak position; D refers to crystallite size; FWHM is full width at half maximum)

C-NiO			P-NiO			Li-NiO		
2 Theta	**FWHM**	**D (nm)**	**2 Theta**	**FWHM**	**D (nm)**	**2 Theta**	**FWHM**	**D (nm)**
37.68	0.82	**10.29**	37.64	0.24	**34.83**	37.93	0.28	**29.73**
43.71	1.01	**8.48**	43.67	0.25	**33.97**	43.96	0.32	**26.79**
63.28	1.26	**7.39**	63.24	0.38	**24.60**	63.53	0.45	**20.67**
75.80	1.40	**7.18**	75.76	0.47	**21.59**	76.05	0.54	**18.77**
79.66	2.42	**4.27**	79.72	0.46	**22.31**	79.98	0.57	**18.11**
Average D (nm)		**7.52**			**27.45**			**22.81**

5.1.2 Chemical – Elemental Composition

Elemental mapping is shown in Figure 5.2 from survey spectra of NiO_x powders measured in a range of binding energy of 0 to 1300 eV. All spectra consist of standard C 1s peak at 285.72 eV and comprise both O 1s and Ni 2p peaks. The C peak seen in the structure comes from the use of the hydrocarbon line located on the sample surface, which is assumed to have a binding energy of 285.72 eV. The characteristic quadruple peak transitions of the NiO phase are observed in the binding energy range of 850 - 890 eV. Peaks at 854 eV, 861 eV, 872 eV and 879 eV are associated with $Ni2p_{3/2}$, and $Ni2p_{1/2}$ scattering, respectively. Besides Li-NiO powders have an extra Li 1s peak at approximately 55 eV in the inset graph of Figure 5.3. The other photoemission intensity peaks such as Ni 3p, Ni 3s, O 1s, Ni $2p_{1/2}$, and Ni $2p_{3/2}$ and auger electron peaks such as Ni KMM, O KLL are obtained in the XPS survey spectrum (Salunkhe et al., 2020). The absence of any other elemental peaks in the spectrum indicates that there are no foreign elements in the sample.

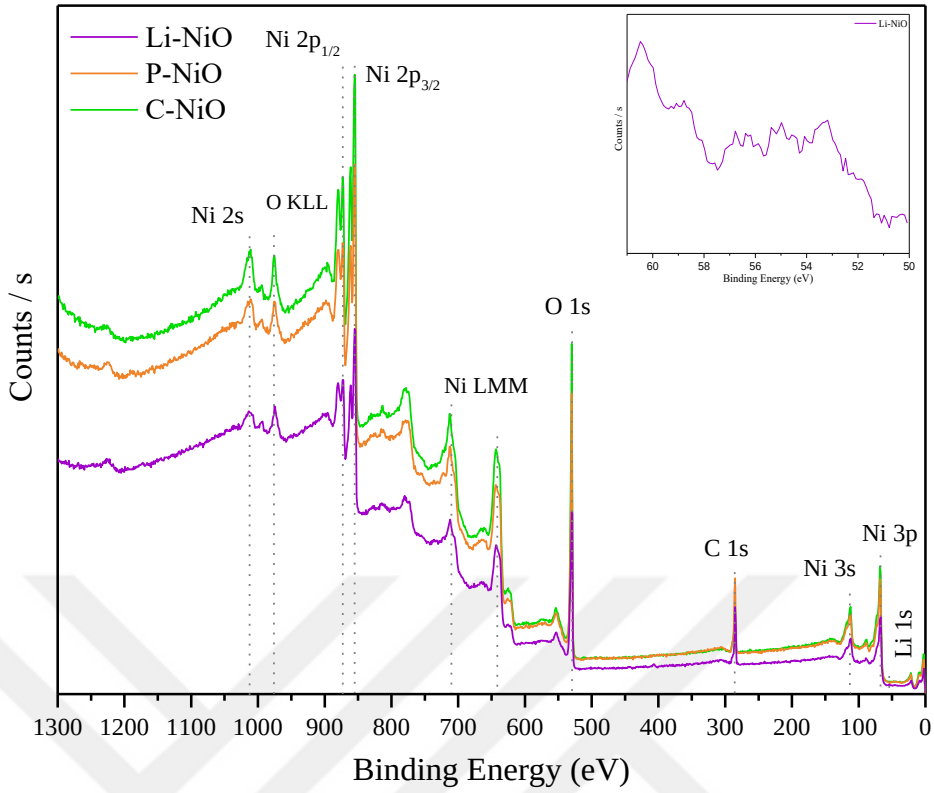

Figure 5.2 Wide survey XPS spectra of all powders

The Ni 2p, O 1s, and C 1s spectra of C-NiO, P-NiO, and Li-NiO are shown in Figure 5.3. The Ni 2p spectra (left of Figure 5.3) included three components: These are Ni^{2+} located at 853 eV, the satellite peak of Ni^{2+} located at 860 eV, and Ni^{3+} located at 855 eV. The O 1s spectra shown in Figure 5.3 (middle column of the figure) contain two peaks at 529 eV and 531 eV, expressing the Ni-O and Ni_2O_3 states. The presence of N^{3+} and Ni^{2+} peaks in the Ni 2p peak indicates that NiO_x is a non-stoichiometric (Tian et al., 2019). The C 1s spectra shown in Figure 5.3 (right column of the figure) contain two peaks at 285 eV and 288 eV, expressing the sp^3 C, and C-O states, respectively. Also, the increase in the magnitude of the Ni^{3+} bonding state was slightly greater than that of the Ni^{2+} bonding state, demonstrating that the electrical properties are enhanced with the annealing (Chang et al., 2006; Diao et al., 2020).

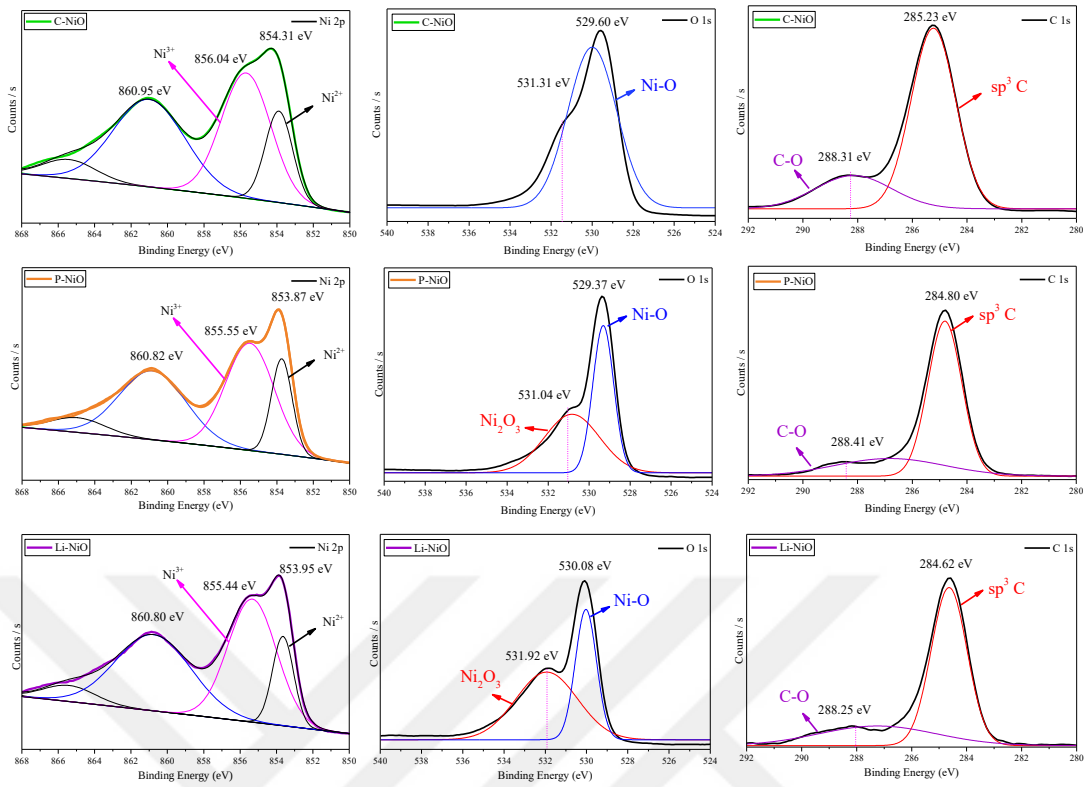

Figure 5.3 Elemental XPS spectra of Ni 2p, O 1s, and C 1s of all powders: The top row of the figure belongs to C-NiO powder, the middle row belongs to P-NiO powder, and the bottom row belongs to Li-NiO powder

5.1.3 Morphological Properties

Scanning electron microscopy is used to create a topographic image of the material by examining the surface of the material. The SEM images of C-NiO and sol-gel derived P-NiO and Li-NiO powders are given in Figure 5.4. While P-NiO and Li-NiO powders were heat-treated at 650 °C, C-NiO was used as supplied. Due to the application of heat treatment, significant differences in particle size and shape in C-NiO powder have attracted attention (Channu et al., 2012). From the images, it is seen that the particles are highly agglomerated in nature. There are some larger particles because of the smaller particles collecting or even agglomerating. Smaller size randomly distributed grains clearly show and homogeneous spherical shaped particles are seen (Rahdar et al., 2015). However, with the Li dopant entering into the crystal structure, the particles show a more pronounced spherical shape (Bhatt et al., 2020).

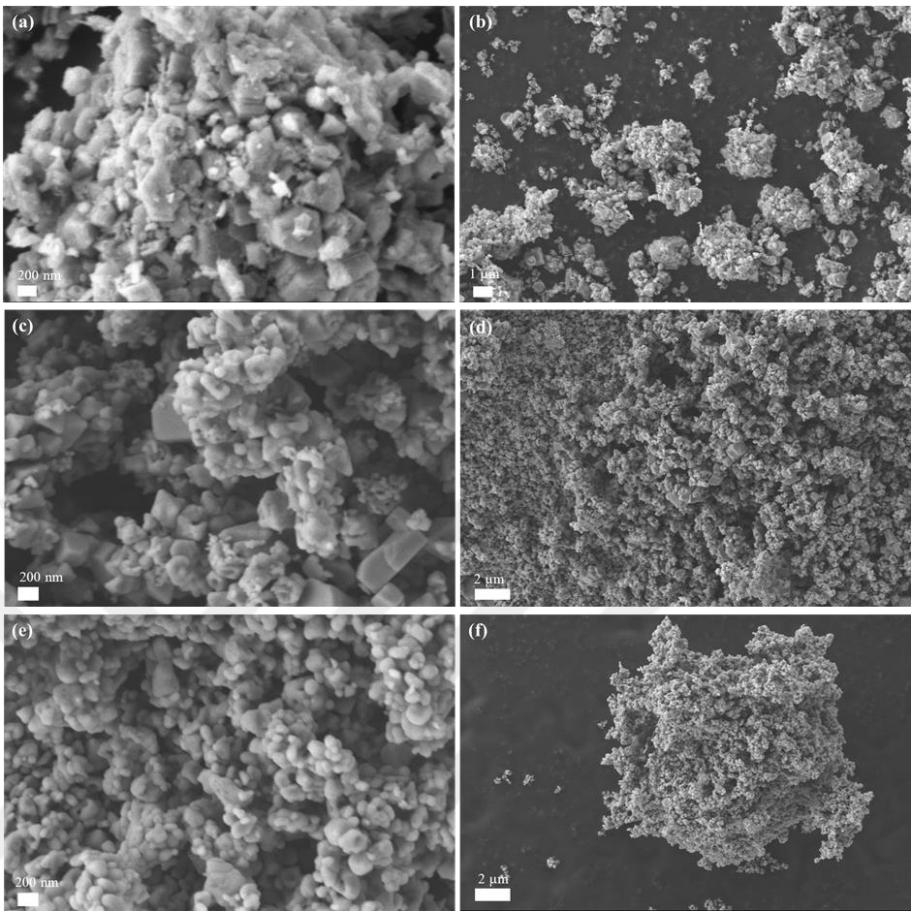

Figure 5.4 SEM images of NiO based powders: a,b) commercially purchased C-NiO, c,d) pristine sol-gel derived P-NiO, e,f) Li-doped sol-gel derived Li-NiO (The images on the left side of the figure were taken at 50K magnification, and the ones on the right at 10K)

5.1.4 Particle Size Properties

The obtained powders C-NiO, P-NiO, and Li-NiO were dispersed in deionized water before measurements. Particle size distributions of C-NiO, P-NiO, and Li-NiO powders were depicted in Figure 5.5. The polydispersity index (PdI) of C-NiO, P-NiO, and Li-NiO were 0.387, 0.402, and 0.337, respectively. As seen in the particle size-density graph, all powders had a polydisperse character because they have peaks in more than one region from the nanometer scale to the submicron scale. The Z-average of C-NiO, P-NiO, and Li-NiO is calculated as 424.7, 1052, and 805.7, respectively. This result proves that larger particles are formed due to the clustering of smaller

particles we see when we examine the SEM images of powder (See *5.1.3. Morphological Properties*). If Z-average is higher than 500 nm, it can only be deduced that there are big aggregates in suspension but the numerical value is usually meaningless. Large particle's peaks higher than small particles because large particles scatter much more light than small particles, the intensity of scattering of a particle is proportional to the sixth power of its diameter (from Rayleigh's approximation) (Niskanen et al., 2019).

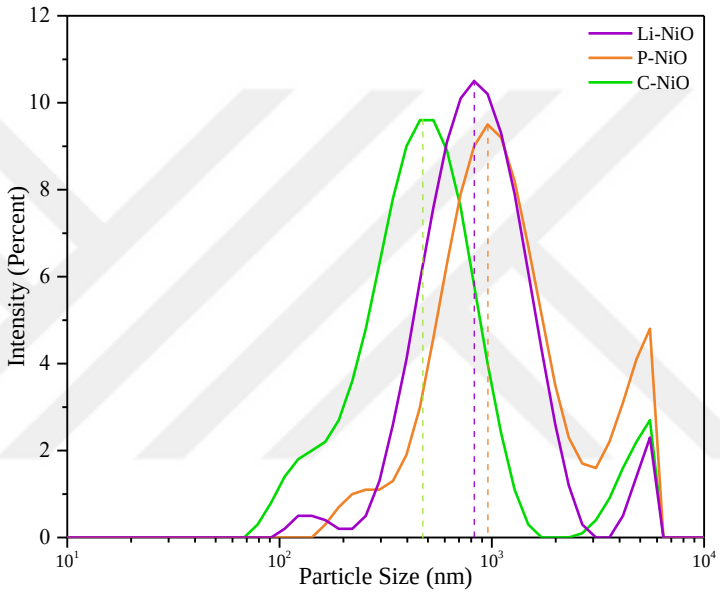

Figure 5.5 Particle size distribution of C-NiO, P-NiO, and Li-NiO. The Dash line represents the Z-average of each powder

5.2 Characterization of Target Materials

5.2.1 Structural Properties

After the powders were pelletized and sintered at 1300 °C for 12 hours, XRD analysis was performed to examine whether there was a change in the phase structure. Figure 5.6 shows the XRD diffraction pattern of NiO_x based targets. According to the results of the analysis, no phase change was observed in the structure, and an increase in intensity was observed in characteristic some peaks due to sintering. The

characteristic peaks of cubic NiO_x structure are located at 37°, 43°, 62°, 76°, and 79°. The peaks match the JCPDS card no. 04-0835 as in the powders form.

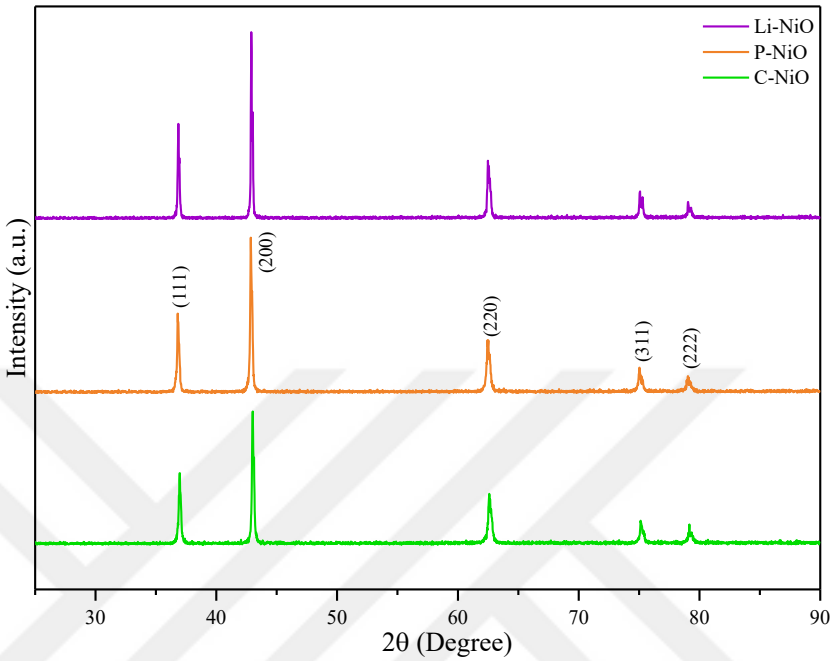

Figure 5.6 XRD patterns of C-NiO, P-NiO, and Li-NiO target materials

5.2.2 Chemical – Elemental Composition

Although no crystal phase other than NiOx was detected using XRD, X-Ray Photoelectron Spectroscopy (XPS) measurements were applied to investigate the chemical components of the pristine and the Li doped NiOx target materials. The XPS survey spectra for the C-NiO, P-NiO, and Li-NiO target materials are shown in Figure 5.7. All spectra consist of standard C 1s peak at 285.72 eV and comprise both O 1s and Ni 2p peaks. Also, Li-NiO powders have an extra Li 1s peak at approximately 56 eV in the inset graph of Figure 5.7. If the powder and target plots of Li-NiO are compared to see the effect of Li additive, it is observed that the Li 1s peak can be seen more clearly with the effect of the heat treatment (Chang et al., 2020). Also, unfortunately, Sn peak between 486-496 eV is seen in P-NiO target material. In this case, the sintered furnace is considered to be contaminated as there are no peaks of the

element Sn in the powder form of P-NiO. The peak of Ni $2p_{3/2}$ at 857.8 eV and the O 1s level at 531.3 eV corresponds to the Ni^{3+} state of the Ni_2O_3. In addition, the presence of the Ni^{2+} state of NiO_x is revealed by the Ni $2p_{3/2}$ level at around 855 and O 1s level at 529 eV peaks. The coexistence of Ni^{2+} and Ni^{3+} states is a confirmation of the non-stoichiometric nature of the NiO_x (Alkarsifi et al., 2020).

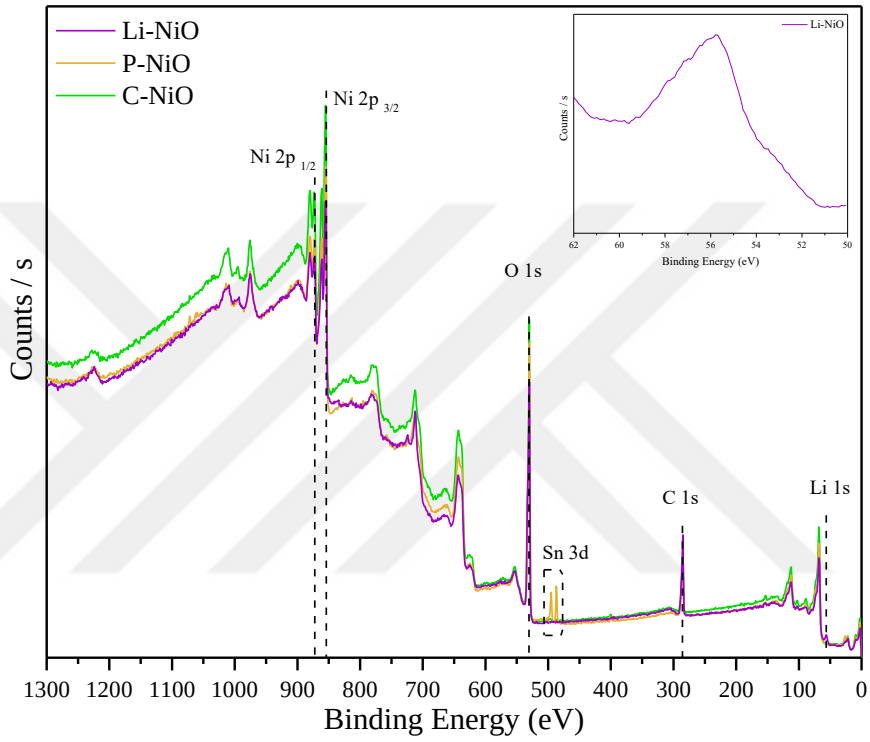

Figure 5.7 Wide survey XPS spectra of all target materials

5.2.3 Morphological Properties

The SEM images of the surfaces of C-NiO, P-NiO, and Li-NiO target materials obtained as a result of sintering application are given in Figure 5.8. Sintering is the bonding of particles that are in contact with each other by diffusion at high temperatures. According to this; as a result of the sintering process, condensation and strength increase occur in green compact (Burke, 2013). It shows that a slight increment in the average pellet grain size (D_{grain}) compared to $D_{particle}$ was mainly due to sintering. The peeling appearance on the target material surfaces is the result of

grinding the surface after sintering to remove surface roughness and clean it. If the SEM view of the three target materials is examined, the low porosity in Li-NiO is explained by the increase in grain size with sintering. Moreover, the grain sizes are homogeneously distributed and the grain shape is approximately spherical (Cosentino & Muccillo, 2002).

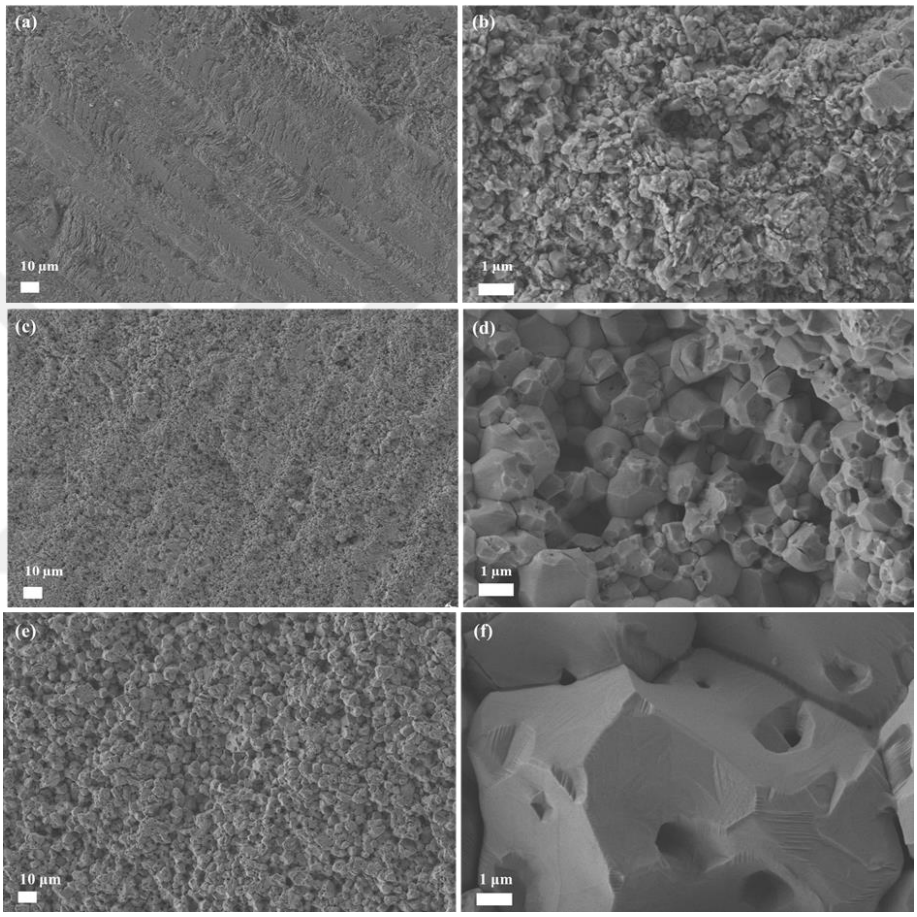

Figure 5.8 SEM images of NiO based target materials: a,b) commercially purchased C-NiO, c,d) pristine sol-gel derived P-NiO, e,f) Li-doped sol-gel derived Li-NiO (The images on the right side of the figure were taken at 20K magnification, and the ones on the left at 1K)

5.2.4 Determination of Density

Pellets were produced from the commercial and sol-gel NiO-based powders obtained by a hydraulic press to preform. The preformed pellets were kept in the CIP device under 250 MPa pressure for 30 minutes. The green pellets were sintered at 1300 °C for 12 hours in air at a heating rate of 2.5 °C/min from room temperature upto 600 °C and 5 °C/min to 1300 °C and cooling down to room temperature (Sahu et al., 2020; Sahu et al., 2017). Both the CIP process with high pressure and the sintering process with high-temperature were applied to the target materials for removing porosities and to make them denser which are important criteria of magnetron sputtering targets. During the sintering process, there are many repulsive forces such as van de Walls force, electrostatic force, chemical bonding force and electronic force that accelerate the contact of particles with each other. Atomic diffusion increases with the increase in temperature. Thus, two surface atoms can more easily cross the potential barrier for chemical bonding. Therefore, the effect of temperature on relative density is very important (Wang et al., 2011). The quality and and surface composition of target materials is the most important key to efficient thin film production. In the RF magnetron sputtering method; the sintering density, microstructural uniformity, stoichiometry, grain size, elektrical and mechanical properties of target material significantlyaffects the sputtering process and the properties of the deposited thin-films (Fang et al., 2002).

The weight of the target materials obtained after sintering was measured to determine the density via Archimedes' Principle. The dry weight (W_K) in air of C-NiO, P-NiO, and Li-NiO target materials were measured as 1.624 g, 1.807 g, and 1.805g. While the water- suspended weight (W_A) of the water-impregnated target materials C-NiO, P-NiO, and Li-NiO were measured as 1.378 g, 1.529 g, and 1.520 g; their weight of air (W_D) were measured as 1.636 g, 1.821 g, and 1.815 g, respectively. As a result of this measurements, the apprent solid densities of the C-NiO, P-NiO, and Li-NiO pellets were measured 6.59, 6.51, and 6.34, respectively. The bulk densities of the C-NiO, P-NiO, and Li-NiO pellets were measured 6.28, 6.21, and 6.12, respectively. (These densities calculation formulas are explained in detail in the Experimental Details, *4.5.5. Determination of Density*). When apparent solid density results were

compared with the bulk density results, the bulk density ratio of the pellets obtained were found to be 95.2%, 95.3%, and 96.5%. The observed particle coalescence is consistent with the bulk density ratio of 96.5% Li-NiO (compared to the apparent solid density of 6.34 g / cm^3 NiO) of the pellet bulk density (6.12 g / cm^3). Generally, the increase in density of the sample after sintering indicates a significant reduction in the Ni_2O_3 impurity phase in the resulting pellet compared to the powder density measured for NiO nanoparticles. In addition; it is known that Ni_2O_3 decomposes into NiO with a loss of O_2 around 600 °C. This decomposition reaction also occurs during the sintering process at high temperatures and provides the NiO pellet containing a smaller portion of the Ni_2O_3 phase (Sahoo et al., 2011).

Table 5.2 The theoretical and experimentally calculated density of C-NiO, P-NiO, and Li-NiO target materials

Target Materials	Apperent Solid Density (g/cm^3)	Bulk Density (g/cm^3)	Bulk Density Ratio (%)
C-NiO	6.59	6.28	95.2
P-NiO	6.51	6.21	95.3
Li-NiO	6.34	6.12	96.5

5.3 Characterization of Thin Film

5.3.1 Structural Properties

The XRD graph of NiO-based films deposited on glass / ITO with the three different target materials obtained is given in Figure 5.9. The six peaks at 21.6°, 30.4°, 35.4°, 45.5°, 50.9°, and 60.5° which are related to the sequent planes (211), (222), (400), (431), (440), and (622) respectively belong to the glass / ITO material used as a substrate for film deposition. It shows good agreement with the JCPDS card no. 71-2195 of the cubic In_2O_3:Sn structure (ITO) (Souici et al., 2019). When the graph is examined, the X-ray diffraction patterns of deposited NiO thin films only show a major diffraction peak at $2\theta = 43°$, which is associated with the (200) plane. However, the NiO crystal structure has more diffraction peaks (5 peaks) (See 5.1.1. *Structural*

Properties). There is a peak (200) with 2θ = 43° in the entire spectrum, the most intense peak given in the JCPDS card no. 04-0835. The reason for occurring only at the peak at 43 degrees is that thin films are deposited at room temperature and not heat-treated after deposition. (Suman Nandy, Saha, Mitra, & Chattopadhyay, 2007b; Souici et al., 2019; Yang et al., 2019).

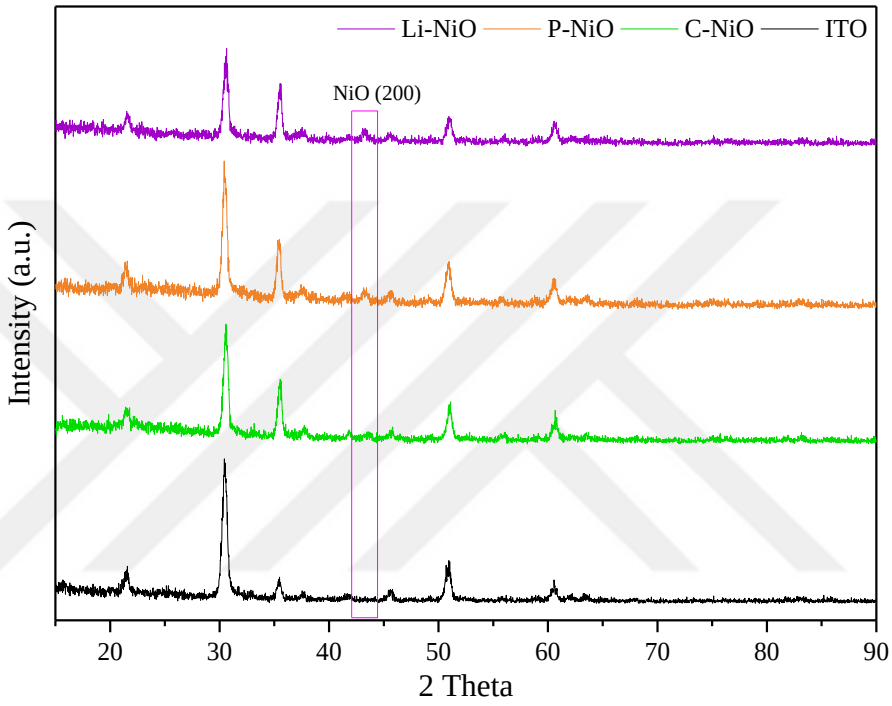

Figure 5.9 XRD graph of glass / ITO and NiO based films deposited on glass / ITO

5.3.2 Chemical – Elemental Composition

The elemental mapping was carried out from the wide survey spectra of NiO based films measured over a binding energy range of 0 to 1300 eV and the graph is displayed in Figure 5.10. A standard carbon peak C1s at 284.80 eV was observed in the spectra as the reference peak for all the samples and it includes Ni $2p_{3/2}$, Ni $2p_{1/2}$ O 1s, and also Li 1s peaks. There are no other fundamental peaks in the spectra, which clearly indicates that the deposited films do not contain any foreign elements in the sample, except fluorine at 685.12 eV. It was decided that the thin films contain fluorine because the HF acid used during the cleaning of the vacuum chamber of the sputtering system was not removed well (Salunkhe et al., 2020).

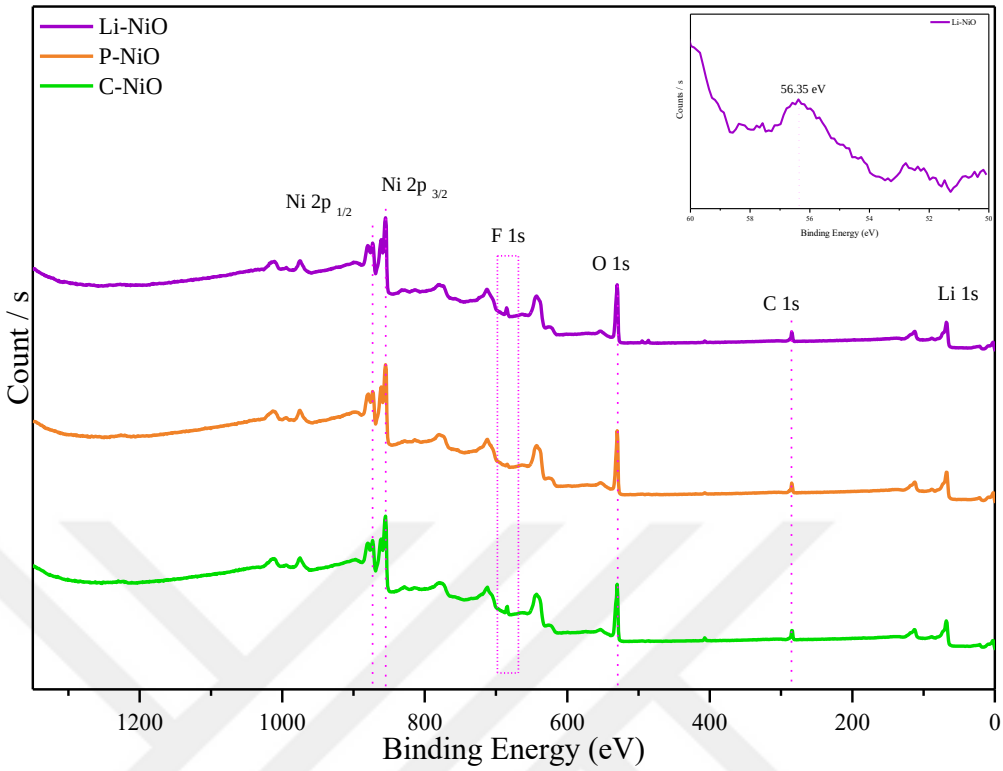

Figure 5.10 Wide survey XPS spectra of all thin films

The XPS spectra of the Ni $2p_{3/2}$ states of NiO thin films deposited with the same parameter in Figure 5.11. The Ni 2p spectra involved three components. The peaks at around 854 eV were attributed to Ni^{2+}, and the peak at around 861 eV is their satellite peak. The peak at 855 eV was appointed to Ni^{3+} (Lei et al., 2014). The O 1s spectra shown in Figure 5.11 (left side) included two peaks at 529 and 531 eV, corresponding to Ni–O, and Ni_2O_3, respectively. With the use of different NiO based target, if the magnitude of the Ni^{3+} binding state is slightly larger than the Ni^{2+} binding state, this indicates that the hole carrier concentration of thin films is increased. In the O 1s XPS spectra, the deconvolution of the electron binding energy of NiO (529.3 eV) and Ni_2O_3 (531 eV) was observed for the NiO based thin films (Chang et al., 2006; Suman Nandy et al., 2007; Yu et al., 2003). By the way, O1s XPS spectra of NiO thin films with Ni $2p_{3/2}$ results were confirmed that these films are p-type films and the coexistence of Ni^{2+} and Ni^{3+} peaks is evidence of the non-stoichiometric nature of the oxygen-rich NiO film. (Salunkhe et al., 2020).

After lithium doping, the XPS spectra of Ni 2p of Li-Ni remained virtually unchanged, indicating similar Ni components with the intact C-NiO and P-NiO samples. However, after doping, an obvious change in the O 1s core level is observed. Figure 5.11 (pink line to the left of the figure) shows the XPS spectra for O 1s in the P-NiO film, with the peak centered at 529.42 eV, confirming the octahedral bond of Ni-O. Interestingly, the O 1s peaks for Li-NiO film show a binder energy shift towards the lower energy direction compared to that in the NiO film. Chemical impurities other than NiO can cause XPS peak shift and asymmetry. These phenomena indicate that Li is successfully involved and causes lattice changes (Qiu et al., 2017).

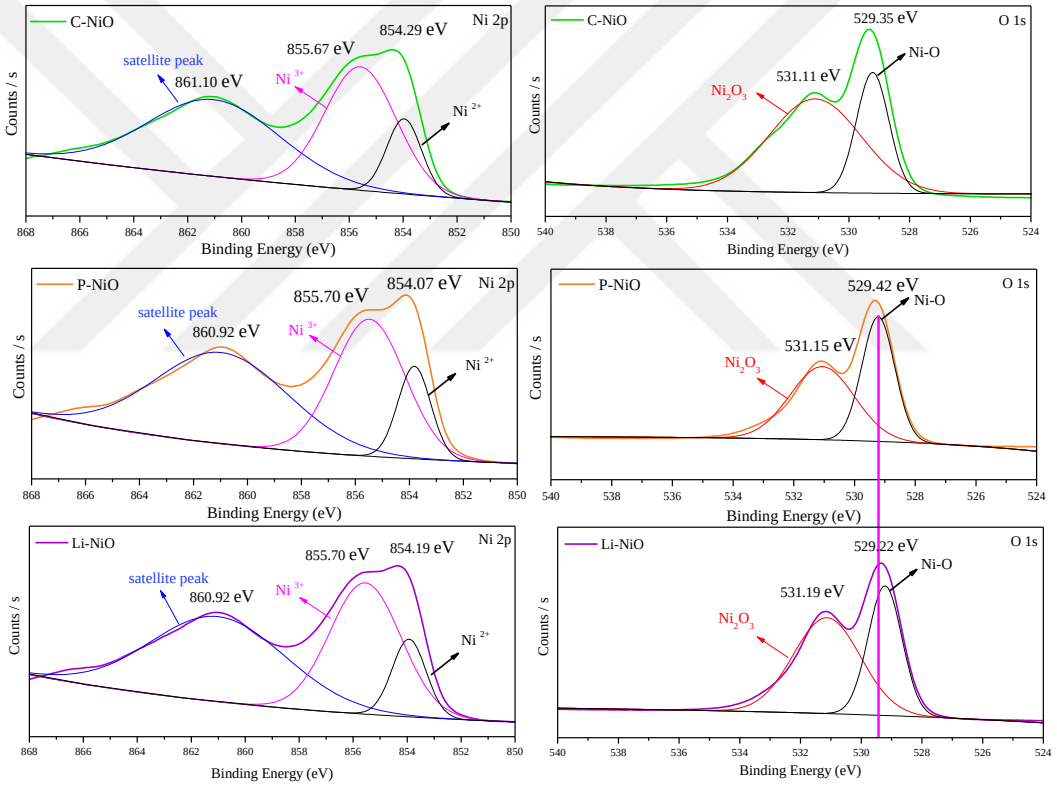

Figure 5.11 Elemental XPS spectra of Ni 2p, and O 1s of all thin films: The top row of the figure belongs to C-NiO, the middle row belongs to P-NiO, and the bottom row belongs to Li-NiO thin films

5.3.3 Morphological Properties

The SEM images of NiO-based thin films deposited with the target materials obtained in the RF magnetron sputtering system and glass/ ITO material used as a

substrate are given in Figure 5.12. The column on the right of the figure gives the top-view of the films and the column on the left shows the section-view of films. When the images of C-NiO, P-NiO, and Li-NiO thin films were examined, it is seen that the films are coated homogeneously but have a rough surface. This is because the films are used as-prepared and not subjected to heat treatment. The particle sizes of C-NiO, P-NiO, and Li-NiO are almost identical compared to that of ITO (Qiu et al., 2017; Wang et al., 2020). When the left side of the graph is examined, the section-view image taken to determine the thickness of the films on the glass/ITO is seen. The thicknesses of the ITO, C-NiO, P-NiO, and Li-NiO films were measured approximately as 70 nm, 110 nm, 150 nm, and 230 nm, respectively. The reason for the different thicknesses of thin films C-NiO, P-NiO, and Li-NiO deposited at the same sputtering parameters can be show as the sputtering rate (Hotový et al., 1998).

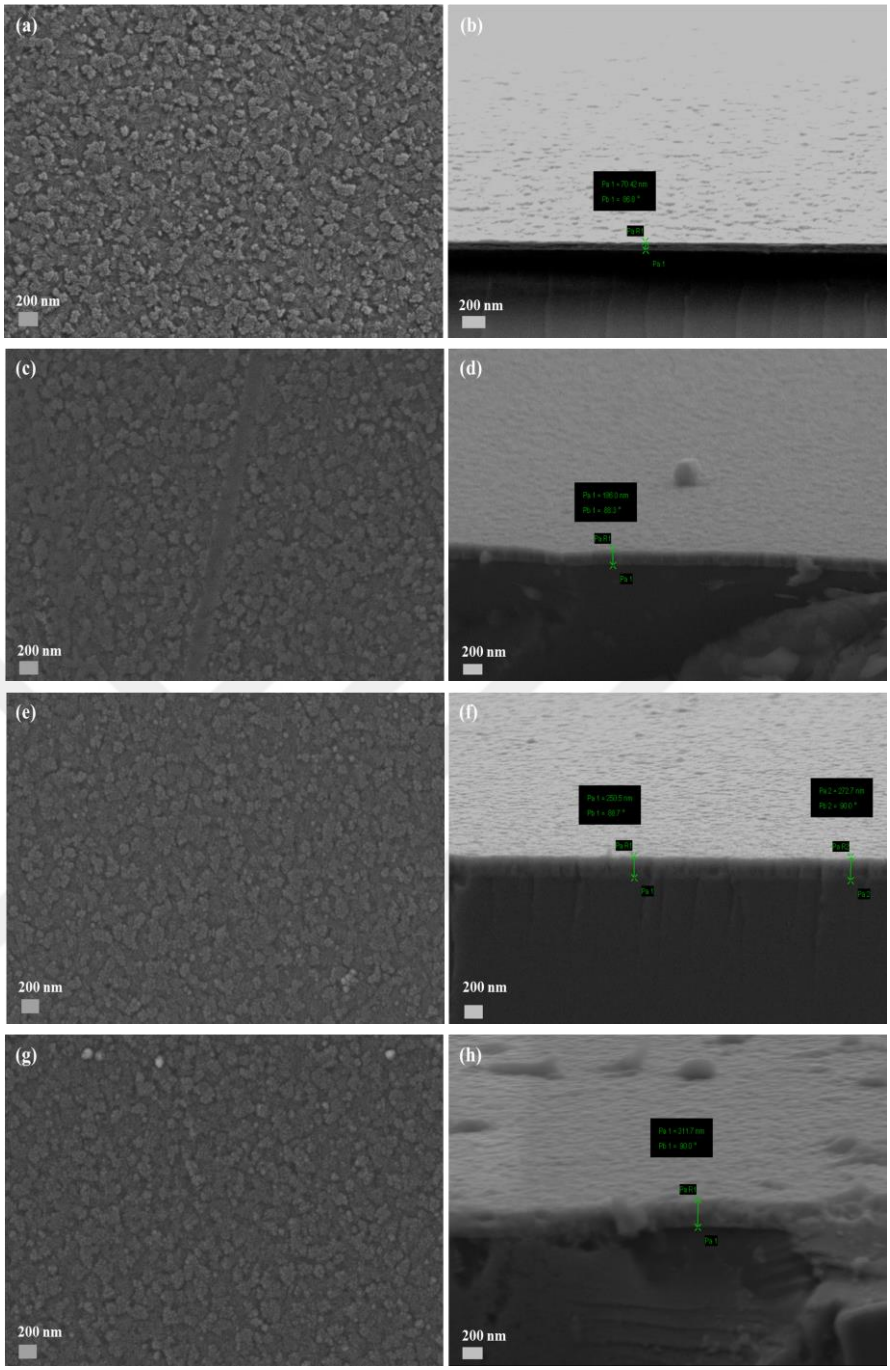

Figure 5.12 SEM images of NiO based thin films: a,b) glass/ ITO used as a substrate for thin films c,d) commercially purchased C-NiO, e,f) pristine sol-gel derived P-NiO, g,h) Li-doped sol-gel derived Li-NiO (The images on the left side of the top view were taken at 50K magnification, and the right of the cross-section view were taken at 50K)

CHAPTER SIX
CONCLUSION AND FUTURE WORKS

In this study, synthesis of pristine and lithium doped NiO_x based powders by sol-gel technique, NiO_x based target materials by cold isostatic press, and NiO_x based thin films by RF sputtering method were investigated with the goal of achieving structural analysis. Before obtaining the target materials, powder production was optimized. The green transparent solutions were successfully prepared with nickel nitrate, lithium nitrate, and methanol. After the solution was gelled with the help of heat, the gelled form was ground in a mortar and heat-treated at 600 °C. The combustion process of organic groups occurred at ~350 °C as a second thermal phenomenon. The last phenomenon was the formation of ceramic oxides at temperatures between 450 and 500 °C. The significant amount of these weight losses was observed during the combustion and oxidation reactions. The Z-average of C-NiO, P-NiO, and Li-NiO powders were calculated as 424.7, 1052, and 805.7, respectively. NiO_x based target materials consisting of powders were sintered at 1300 °C for 12 hours after CIP under 250 MPa pressure for 30 minutes. The densities of C-NiO, P-NiO and Li-NiO target materials obtained after sintering are 95.2%, 95.3%, and 96.5%. The NiO_x based films were deposited on glass/ITO substrates from sol-gel derived NiO_x based target materials by using RF magnetron sputtering. The films obtained are the same as they were deposited and all the analyzes applied were applied without heat treatment. The thicknesses of the ITO, C-NiO, P-NiO, and Li-NiO films were measured approximately as 70 nm, 110 nm, 150 nm, and 230 nm, respectively. The reason for the different thicknesses of thin films C-NiO, P-NiO, and Li-NiO deposited at the same sputtering parameters can be shown as the sputtering rate. The XRD results showed that the polycrystallinity did not change with Li doping of NiO_x, except for a slight shift. XPS analysis have also proved that the structure is NiO doped with Li as desired. In the characterization of the SEM, both powders, targets and thin films were analyzed and necessary measurements were made to determine their sizes. The thicknesses of the ITO, C-NiO, P-NiO, and Li-NiO films were measured approximately as 70 nm, 110 nm, 150 nm, and 230 nm, respectively.

Future work may involve the heat-treatment of NiO_x-based films after deposition. In addition to this study, a perovskite solar cell can be produced using the obtained HTMs for future studies. Even produced HTMs can be developed with different additive ratios and different additive materials. These additives can be produced as single or codoped, while paying attention to the band gap values, as well as optical, charge carrying and electron blocking properties of the HTM layer.

REFERENCES

Abdollahi Nejand, B., Ahmadi, V., & Shahverdi, H. R. (2015). new physical deposition approach for low cost inorganic hole transport layer in normal architecture of durable perovskite solar cells. *ACS Applied Materials and Interfaces*, *7*(39), 21807–21818.

Alkarsifi, R., Avalos-Quiroz, Y. A., Perkhun, P., Liu, X., Fahlman, M., Bharwal, A. K., & Ackermann, J. (2020). Organic–inorganic doped nickel oxide nanocrystals for hole transport layers in inverted polymer solar cells with color tuning. *Materials Chemistry Frontiers*, 1-12.

Angelo, P. C., & Subramanıan, R. (2008). *Powder Metallurgy: Science, technology and applications*. New Delhi: PHI Learning Private Limited.

Antoini, E. (1992). Sintering of LixNi1−xO solid solutions at 1200°C. *Journal of Materials Science*, *27*(12), 3335–3340.

Anttila, O. (2015). Czochralski growth of silicon crystals. In *Handbook of Silicon Based MEMS Materials and Technologies: Second Edition*, 18–55.

Aytimur, A., Koçyiğit, S., & Uslu, İ. (2014). Calcia stabilized ceria doped zirconia nanocrystalline ceramic. *Journal of Inorganic and Organometallic Polymers and Materials*, *24*(6), 927–932.

Başalan, E. (2017). *Magnetron saçtırma ve elektrokimyasal anotlama teknikleri ile elde edilen TiO2 nanoyapıların üretimi, karakterizasyonu ve fotokatalitik uygulamaları*. M.Sc Thesis, Dokuz Eylül University, İzmir.

Bhatt, A. S., Ranjitha, R., Santosh, M. S., Ravikumar, C. R., Prashantha, S. C., Maphanga, R. R., & Silva, G. F. B. L. (2020). Optical and electrochemical applications of Li-doped NiO nanostructures synthesized via facile microwave technique. *Materials*, *13*(13), 1–17.

Brinker, C., & Scherer, G. (2013). *Sol-gel science: The physics and chemistry of sol-gel processing*. Cambridge: Elsevier.

Burke, J. E. (2013). *Progress in ceramic science: Volume 3*. Oxford: Elsevier.

Chang, H. L., Lu, T. C., Kuo, H. C., & Wang, S. C. (2006). Effect of oxygen on characteristics of nickel oxideindium tin oxide heterojunction diodes. *Journal of Applied Physics*, *100*(12), 124503.

Chang, J. Y., Chen, Y. C., Wang, C. M., & Chen, Y. W. (2020). Electrochromic properties of Li-Doped NiO films prepared by RF magnetron sputtering. *Coatings*, *10*(1), 1–8.

Channu, V. S. R., Holze, R., & Rambabu, B. (2012). Synthesis and characterization of NiO nanoparticles for electrochemical applications. *Colloids and Surfaces A: Physicochemical and Engineering Aspects*, *414*, 204–208.

Chen, H. L., Lu, Y. M., & Hwang, W. S. (2005). Characterization of sputtered NiO thin films. *Surface and Coatings Technology*, *198*(1–3), 138–142.

Chen, J., & Park, N. G. (2018). Inorganic hole transporting materials for stable and high efficiency perovskite solar cells. *Journal of Physical Chemistry C*, *122*(25), 14039–14063.

Chen, W., Wu, Y., Liu, J., Qin, C., Yang, X., Islam, A., & Han, L. (2015). Hybrid interfacial layer leads to solid performance improvement of inverted perovskite solar cells. *Energy and Environmental Science*, *8*(2), 629–640.

Cosentino, I. C., & Muccillo, R. (2002). Powder synthesis and sintering of high density thoria-yttria ceramics. *Journal of Nuclear Materials*, *304*(2–3), 129–133.

Danial, A. S., Saleh, M. M., Salih, S. A., & Awad, M. I. (2015). On the synthesis of nickel oxide nanoparticles by sol-gel technique and its electrocatalytic oxidation of glucose. *Journal of Power Sources*, *293*, 101–108.

Diao, C. C., Huang, C. Y., Yang, C. F., & Wu, C. C. (2020). Morphological, optical, and electrical properties of p-type nickel oxide thin films by nonvacuum deposition. *Nanomaterials*, *10*(4), 636.

Dilsiz, N., & Akovali, G. (2002). Study of sol-gel processing for fabrication of low density alumina microspheres. *Materials Science and Engineering A*, *332*(1–2), 91–96.

Dirksen, J. A., Duval, K., & Ring, T. A. (2001). NiO thin-film formaldehyde gas sensor. *Sensors and Actuators B: Chemical*, *80*(2), 106–115.

Dutta, T., Gupta, P., Gupta, A., & Narayan, J. (2010). Effect of Li doping in NiO thin films on its transparent and conducting properties and its application in heteroepitaxial p-n junctions. *Journal of Applied Physics*, *108*(8), 083715.

Erdoğan, M. (2011). *Toprak işleme endüstrüsünde kullanılan çizici kalemlerin mikrodalga toz sinterleme tekniği ile üretimi ve karakterizasyonu*. PhD Thesis, Afyon Kocatepe University, Afyonkarahisar.

Etgar, L. (2016). *Hole conductor free perovskite-based solar cells.* New York: Springer Publishing.

Fang, G. J., Li, D., & Yao, B. L. (2002). Influence of post-deposition annealing on the properties of transparent conductive nanocrystalline ZAO thin films prepared by RF magnetron sputtering with highly conductive ceramic target. *Thin Solid Films,* 418(2), 156-162.

Fu, Q., Tang, X., Huang, B., Hu, T., Tan, L., Chen, L., & Chen, Y. (2018). Recent progress on the long-term stability of perovskite solar cells. *Advanced Science, 5*(5), 1700387.

German Randall M. (2005). *Powder metallurgy and particulate materials processing: the processes, materials, products, properties and applications*. Princeton: Metal Powder Industry Federation.

Gómez, A., Galeano, A., & Saldarriaga, W. (2015). Deposition of YBaCo4O7+ δ thin films on (001)-SrTiO3 substrates by dc sputtering. *Vacuum,* (119), 7–14.

Güler, S. (2016). *Metallere uygulanan mikrodalga ile termal işlemlerin modellenmesi ve bu işlemlerin özelliklere etkisi*. M.Sc Thesis, Dokuz Eylül University, İzmir.

Guo, Y., Jin, Z., Yuan, S., Zhao, J. S., Hao, M. Y., Qin, Y., & Ai, X. C. (2020). Effects of interfacial energy level alignment on carrier dynamics and photovoltaic performance of inverted perovskite solar cells. *Journal of Power Sources, 452,* 227845.

Hamed, M. S. G., & Mola, G. T. (2020). Mixed halide perovskite solar cells : Progress and challenges. *Critical Reviews in Solid State and Materials Sciences*, *45*(2), 85–112.

Heo, J., Im, S., Noh, J., & Mandal, T. (2013). Efficient inorganic–organic hybrid heterojunction solar cells containing perovskite compound and polymeric hole conductors. *Nature*, *7*(6), 486–491.

Hotový, I., Búc, D., Haščík, Š., & Nennewitz, O. (1998). Characterization of NiO thin films deposited by reactive sputtering. *Vacuum*, *50*(1–2), 41–44.

Irwin, M. D., Buchholz, D. B., Hains, A. W., Chang, R. P. H., & Marks, T. J. (2008). p-Type semiconducting nickel oxide as an efficiency-enhancing anode interfacial layer in polymer bulk-heterojunction solar cells. *Proceedings of the National Academy of Sciences of the United States of America*, *105*(8), 2783–2787.

Ishihara, M., Li, S. J., Yumoto, H., & Akashi, K. (1998). Control of preferential orientation of AlN films prepared by the reactive sputtering method. *Thin Solid Films*, *316*(1–2), 152–157.

Jamal, M. S., Shahahmadi, S. A., Chelvanathan, P., Alharbi, H. F., Karim, M. R., Ahmad Dar, M., & Akhtaruzzaman, M. (2019). Effects of growth temperature on the photovoltaic properties of RF sputtered undoped NiO thin films. *Results in Physics*, *14*, 102360.

Jameel, D. A. (2015). Thin film deposition processes. *International Journal of Modern Physics and Applications*, *1*(4), 193–199.

Jeng, J. Y., Chen, K. C., Chiang, T. Y., Lin, P. Y., Tsai, T. Da, Chang, Y. C., & Hsu, Y. J. (2014). Nickel oxide electrode interlayer in CH3NH3PbI 3 perovskite/PCBM planar-heterojunction hybrid solar cells. *Advanced Materials*, *26*(24), 4107–4113.

Khan, K. (2016). *NiOx based device structures*. Doctoral dissertation, University of Toledo, Ohio.

Klar E. (1983). *Powder metallurgy: applications, advantages, and limitations*. Ohio: American Society for Metals, Metals Park.

Kloskowski, A., Pilarczyk, M., Chrzanowski, W., & Namieśnik, J. (2010). Sol-Gel technique -a versatile tool for adsorbent preparation. *Critical Reviews in Analytical Chemistry*, *40*(3), 172–186.

Kuşoğlu, İ. M. (2011). *Demir esaslı metal tozlarından geleneksel ve mikrodalga sinterleme yöntemleri ile malzeme üretimi ve özelliklerinin karşılaştırılması*. PhD Thesis, Dokuz Eylül University, İzmir.

Lee, C. Y., Chiang, C. M., Wang, Y. H., & Ma, R. H. (2007). A self-heating gas sensor with integrated NiO thin-film for formaldehyde detection. *Sensors and Actuators, B: Chemical*, *122*(2), 503–510.

Lei, Y., Li, J., Wang, Y., Gu, L., Chang, Y., Yuan, H., & Xiao, D. (2014). Rapid microwave-assisted green synthesis of 3D hierarchical flower-shaped NiCo2O4 microsphere for high-performance supercapacitor. *ACS Applied Materials and Interfaces*, *6*(3), 1773–1780.

Li, W., Fries, D. P., & Malik, A. (2004). Sol-gel stationary phases for capillary electrochromatography. *Journal of Chromatography A*, *1044*(1–2), 23–52.

Li, X., Bi, D., Yi, C., Décoppet, J., … J. L.-, & 2016, U. (2016). A vacuum flash–assisted solution process for high-efficiency large-area perovskite solar cells. *Science*, *353*(6294), 58–62.

Liu, C., Liu, J., & Wang, Y. (2011). Preparation of indium tin oxide targets with a high density and single phase structure by normal pressure sintering process. *Rare Metals*, *30*(2), 126–130.

Liu, F., Wang, X., Hao, J., Han, S., Lian, J., & Jiang, Q. (2017). High density arrayed ni/nio core-shell nanospheres evenly distributed on graphene for ultrahigh performance supercapacitor. *Scientific Reports*, *7*(1), 1–10.

Liu, Z., Chang, J., Lin, Z., Zhou, L., Yang, Z., Chen, D., …, & Hao, Y. (2018). High-performance planar perovskite solar cells using low temperature, solution–combustion-based nickel oxide hole transporting layer with efficiency exceeding 20%. *Advanced Energy Materials*, *8*(19), 1703432.

Liu, H., Gao, M., Yang, B., Chen, H., Zhang, H., & Zhang, H. (2020). Characteristics

of optimized Al:ZnO sputtering targets prepared by nanostructured powder. *Ceramics International*, 46(5), 6311-6317.

Maurya, D. K., Sardarinejad, A., & Alameh, K. (2014). Recent developments in R.F. magnetron sputtered thin films for ph sensing applications - An overview. *Coatings*, *4*(4), 756–771.

Mitzi, D. B., Feild, C. A., Harrison, W. T. A., & Guloy, A. M. (1994). Conducting tin halides with a layered organic-based perovskite structure. *Nature*, *369*(6480), 467–469.

Miyanaga, M., Watatani, K., Awata, H., Tokuda, K., & Tominaga, A. (2020). U.S. Patent Application No. 16/347,152.

Najafi, M., Di Giacomo, F., Zhang, D., Shanmugam, S., Senes, A., Verhees, W., … & Andriessen, R. (2018). Highly efficient and stable flexible perovskite solar cells with metal oxides nanoparticle charge extraction layers. *Small*, *14*(12), 1702775.

Nandy, S, Goswami, S., & Chattopadhyay, K. K. (2010). Ultra smooth NiO thin films on flexible plastic (PET) substrate at room temperature by RF magnetron sputtering and effect of oxygen partial pressure on their properties. *Applied Surface Science*, *256*(10), 3142–3147.

Nandy, Suman, Saha, B., Mitra, M. K., & Chattopadhyay, K. K. (2007). Effect of oxygen partial pressure on the electrical and optical properties of highly (200) oriented p-type Ni1−xO films by DC sputtering. *Journal of Materials Science*, *42*(14), 5766–5772.

Neves, N., Barros, R., Antunes, E., Ferreira, I., Calado, J., Fortunato, E., & Martins, R. (2012). Sintering behavior of nano- and micro-sized ZnO powder targets for rf magnetron sputtering applications. *Journal of the American Ceramic Society*, *95*(1), 204–210.

Nie, W., Tsai, H., Blancon, J. C., Liu, F., Stoumpos, C. C., Traore, B., & Mohite, A. D. (2018). Critical role of interface and crystallinity on the performance and photostability of perovskite solar cell on nickel oxide. *Advanced Materials*, *30*(5), 1–9.

Niskanen, I., Forsberg, V., Zakrisson, D., Reza, S., Hummelgård, M., Andres, B., … & Thungström, G. (2019). Determination of nanoparticle size using Rayleigh approximation and Mie theory. *Chemical Engineering Science, 201*, 222–229.

Oflaz, M. D. (2019). *Manganese doped solution processed nickel oxide hole transport layer for perovskite solar cells*. M.Sc Thesis, Middle East Technical University, Ankara.

Ozkan, Z. E., Turhan, I., Tepehan, F. Z., & Ozer, N. (2008). Sol-gel deposited nickel oxide films for electrochromic applications. *Solar Energy Materials and Solar Cells*, *92*(2), 164–169.

Pae, S. R., Byun, S., Kim, J., Kim, M., Gereige, I., & Shin, B. (2018). Improving uniformity and reproducibility of hybrid perovskite solar cells via a low-temperature vacuum deposition process for NiOx hole transport layers. *ACS Applied Materials and Interfaces*, *10*(1), 534–540.

Par PARK, D. H. (2010). *Optimization of nickel oxide-based electrochromic thin films*. Doctoral dissertation, L'université Bordeaux, Bordeaux.

Park, J. H., Seo, J., Park, S., Shin, S. S., Kim, Y. C., Jeon, N. J., …& Seok, S. Il. (2015). Efficient CH3NH3PbI3 perovskite solar cells employing nanostructured p-type NiO electrode formed by a pulsed laser deposition. *Advanced Materials*, *27*(27), 4013–4019.

Park, M. A., Park, I. J., Park, S., Kim, J., Jo, W., Son, H. J., & Kim, J. Y. (2018). Enhanced electrical properties of Li–doped NiOx hole extraction layer in p–i–n type perovskite solar cells. *Current Applied Physics*, *18*, 55–59.

Philipps, S., Burger, B., Kiefer, K., & Kost, C. (2018). *Photovoltaics Report*. Retrieved December 12, 2020, from https://www.ise.fraunhofer.de/content/dam/ise/de/documents/publications/studies/Photovoltaics-Report.pdf

Pitchaiya, S., Natarajan, M., Santhanam, A., Asokan, V., Yuvapragasam, A., Madurai Ramakrishnan, V., & Velauthapillai, D. (2020). A review on the classification of organic/inorganic/carbonaceous hole transporting materials for perovskite solar cell

application. *Arabian Journal of Chemistry*, *13*(1), 2526–2557.

Qiu, Z., Gong, H., Zheng, G., Yuan, S., Zhang, H., Zhu, X., … & Cao, B. (2017). Enhanced physical properties of pulsed laser deposited NiO films via annealing and lithium doping for improving perovskite solar cell efficiency. *Journal of Materials Chemistry C*, *5*(28), 7084–7094.

Rahaman, M. N. (2017). *Ceramic processing and sintering* (Vol. 1.). Boca Raton: CRC press.

Rahdar, A., Aliahmad, M., & Azizi, Y. (2015). NiO Nanoparticles: synthesis and characterization. *Journal of Nanostructures*, *5*(2), 145–151.

Ranabhat, K., Patrikeev, L., Revina, A. A. evna, Andrianov, K., Lapshinsky, V., & Sofronova, E. (2016). An introduction to solar cell technology. *Journal of Applied Engineering Science*, *14*(4), 481–491.

Ryu, H. W., Choi, G. P., Lee, W. S., & Park, J. S. (2004). Preferred orientations of NiO thin films prepared by RF magnetron. *Journal of Materials Science*, *39*(13), 4375–4377.

Sahoo, P., Misra, D. K., Salvador, J., Makongo, J. P. A., & Chaubey, G. S. (2011). Microstructure and thermal conductivity of surfactant-free NiO nanostructures. *Journal of Solid State Chemistry*, *190*, 29–35.

Sahu, D. R., Lee, Y., Wu, T., Wang, S., & Huang, J. (2020). Synthesis and electrochromic property improvement of NiO films for device applications. *Thin Solid Films*, *707*, 138097.

Sahu, D. R., Wu, T., Wang, S., & Huang, J. (2017). Electrochromic behavior of NiO films prepared by e-beam evaporation. *Journal of Science: Advanced Materials and Devices*, *2*(2), 225–232.

Salunkhe, P., A.V, M. A., & Kekuda, D. (2020). Investigation on tailoring physical properties of nickel oxide thin films grown by dc magnetron sputtering. *Materials Research Express*, *7*(1), 016427.

Sarialtin, H., Geyer, R., & Zafer, C. (2020). Environmental assessment of transparent

conductive oxide-free efficient flexible organo-lead halide perovskite solar cell. *Energy Sources, Part A: Recovery, Utilization and Environmental Effects*, 1–10.

Sarıtaş, S., Türker, M., & Durlu, N. (2007). Toz metalurjisi ve parçacıklı malzeme işlemleri. *Türk Toz Metalutjisi Derneği Yayınları*, *5*, 2–34.

Shi, Z., & Jayatissa, A. H. (2018). Perovskites-based solar cells: a review of recent progress, materials and processing methods. *Materials*, *11*(5), 729.

Sönmezoğlu, S., Koç, M., & Akın, S. (2012). İnce film üretim teknikleri. *Erciyes Üniversitesi Fen Bilimleri Enstitüsü Fen Bilimleri Dergisi*, *28*(5), 389–404.

Souici, F. Z., Benhaoua, B., Saïdi, H., Boujmil, M. F., Rahal, A., Benhaoua, A., & Aida, M. S. (2019). Influence of rapid thermal annealing in argon atmosphere on properties of electrodeposited cuinse 2 thin films: structural and optical stady. *Chalcogenide Letters*, *16*(2), 79–87.

Subbiah, A. S., Halder, A., Ghosh, S., Mahuli, N., Hodes, G., & Sarkar, S. K. (2014). Inorganic hole conducting layers for perovskite-based solar cells. *Journal of Physical Chemistry Letters*, *5*(10), 1748–1753.

Suzuki, Y., & Teranishi, K. (2009). *Patent No. 7,575,661*, Washington, DC, US.

Thitinun, S., Thanabodeekij, N., Jamieson, A. M., & Wongkasemjit, S. (2003). Sol-gel processing of spirosilicates. *Journal of the European Ceramic Society*, *23*(3), 417–427.

Tian, Y., Gong, L., Qi, X., Yang, Y., & Zhao, X. (2019). Effect of substrate temperature on the optical and electrical properties of nitrogen-doped NiO thin films. *Coatings*, *9*(634), 634.

Toygun, Ş., Köneçoğlu, G., & Kalpaklı, Y. (2013). General principles of sol - gel. *Journal of Engineering and Natural Sciences*, (212), 456–476.

Ün, N. S. (2008). *Development of sol-gel derived hydroxyapatite- titania coatings*. M.Sc Thesis, Middle East Technical University, Ankara.

Upadhyaya, G. S. (1997). *Powder metallurgy technology*. Cambridge: Cambridge International Science Publishing.

Usha, K. S., Sivakumar, R., Sanjeeviraja, C., Sathe, V., Ganesan, V., & Wang, T. Y. (2016). Improved electrochromic performance of a radio frequency magnetron sputtered NiO thin film with high optical switching speed. *RSC Advances*, *6*(83), 79668–79680.

Wang, X. M., Xue, B., Duan, H. Y., Shi, Z. X., Jing, S. U. N., Lu, S. G., & Huang, S. T. (2011). Preparation of Al-doped ZnO sputter target by hot pressing. *Transactions of Nonferrous Metals Society of China*, 21(7), 1550-1556.

Wang, K. C., Shen, P. S., Li, M. H., Chen, S., Lin, M. W., Chen, P., & Guo, T. F. (2014). Low-temperature sputtered nickel oxide compact thin film as effective electron blocking layer for mesoscopic NiO/CH3NH3PbI3 perovskite heterojunction solar cells.*ACS applied materials & interfaces*,6(15), 11851-11858.

Wang, M., Zhu, W., Yin, Z., Huang, L., & Li, J. (2020). Synergistic effects of Li-doped NiOx film prepared by low-temperature combustion as hole-injection layer for high performance OLED devices. *Organic Electronics*, *85*, 105823.

Wei, Z., Qiao, H., Yang, H., Zhu, L., & Yan, X. (2009). Preparation and characterization of NiO nanoparticles by anodic arc plasma method. *Journal of Nanomaterials*, 1–5.

Woodhouse, M., Smith, B., Ramdas, A., & Margolis, R. (2019). *Crystalline silicon photovoltaic module manufacturing costs and sustainable pricing: 1H 2018 Benchmark and Cost Reduction Road Map*. Golden, CO (United States): National Renewable Energy Lab.(NREL).

Xu, L., Chen, X., Jin, J., Liu, W., Dong, B., Bai, X., & Reiss, P. (2019). Inverted perovskite solar cells employing doped NiO hole transport layers: A review. *Nano Energy*, *63*, 103860.

Yang, P., Wang, J., Zhao, X., Wang, J., Hu, Z., Huang, Q., & Yang, L. (2019). Magnetron-sputtered nickel oxide films as hole transport layer for planar heterojunction perovskite solar cells. *Applied Physics A MAterials Science & Processing*, *3*(10), 2–7.

Yin, X., Chen, P., Que, M., Xing, Y., Que, W., Niu, C., & Shao, J. (2016). Highly

efficient flexible perovskite solar cells using solution-derived NiOx hole contacts. *ACS Nano*, *10*(3), 3630–3636.

Yu, G. H., Zhu, F. W., & Chai, C. L. (2003). X-ray photoelectron spectroscopy study of magnetic films. *Applied Physics A: Materials Science and Processing*, *76*(1), 45–47.

Zhang, J. Y., Li, W. W., Hoye, R. L. Z., MacManus-Driscoll, J. L., Budde, M., Bierwagen, O., & Zhang, K. H. L. (2018). Electronic and transport properties of Li-doped NiO epitaxial thin films. *Journal of Materials Chemistry C*, *6*(9), 2275–2282.

Zheng, J., Hu, L., Yun, J. S., Zhang, M., Lau, C. F. J., Bing, J., & Chen, C. (2018). Solution-processed, silver-doped NiO x as hole transporting layer for high-efficiency inverted perovskite solar cells. *ACS Applied Energy Materials*, 1(2), 561-570.

APPENDICES

APPENDIX 1: ABBREVIATIONS

DSSC: Dye-Sensitized Solar Cell

PSC: Perovskite Solar Cell

TCO: Transparent Conductive Oxide

ETM: Electron Transport Material

HTM: Hole Transport Material

Psk: Perovskite Material

VB: Valance Band

CB: Conduction Band

$MAPbI_3$: Methylammonium Lead Iodide

CVD: Chemical Vapor Deposition

PVD: Physical Vapor Deposition

RF: Radio Frequency

PM: Powder Metallurgy

HIP: Hot Isostatic Press

CIP: Cold Isostatic Press

XRD: X-Ray Diffraction

SEM: Scanning Electron Microscopy

XPS: X-Ray Photoelectron Spectroscopy

PDS: Particle Size Distrubition